UNIVERSITY OF OKLAHOMA

GRADUATE COLLEGE

SEISMIC ATTRIBUTE ILLUMINATION OF TECTONIC DEFORMATION IN CHICONTEPEC BASIN, MEXICO

A THESIS

SUBMITTED TO THE GRADUATE FACULTY

in partial fulfillment of the requirements for the

Degree of

MASTER OF SCIENCE

By

ONUR MUTLU
Norman, Oklahoma
2014

SEISMIC ATTRIBUTE ILLUMINATION OF TECTONIC DEFORMATION IN CHICONTEPEC BASIN, MEXICO

A THESIS APPROVED FOR THE
CONOCOPHILLIPS SCHOOL OF GEOLOGY AND GEOPHYSICS

BY

_____
Dr. Kurt J. Marfurt, Chair

_____
Dr. Shankar Mitra

_____
Dr. Jamie Rich

This thesis is dedicated to my spouse Pelin Mutlu, and all my family and friends.

Acknowledgements

I wish to thank my advisor Dr. Kurt J. Marfurt and committee members Dr. Shankar Mitra and Dr. Jamie Rich for their continuous help and support through my graduate studies. I must thank to PEMEX Exploración y Producción for providing the data used in this thesis.

I thank all the contributors of the Attribute-Assisted Seismic Processing and Interpretation (AASPI) Consortium. Special thanks to Landmark (ProMAX), Schlumberger (Petrel), CGG (Hampson-Russell), and Tesseral for providing licenses for the software that were used in this work.

I would like to thank Tengfei Lin, Thang Ha, Sumit Verma, Bo Zhang, and all my friends for their constant support and guidance during my thesis work.

I would like to specially thank my father Riza Haluk Mutlu, my mother Gulbin Mutlu, my brother Can Mutlu, and all my family for their endless support and encouragement in every step of my life. I deeply thank my spouse Pelin Mutlu for her unconditional support and patience. Her support enabled me to finish my research and progress towards the goal to get a Master of Science degree. Finally, I specifically thank my upcoming son for making me extremely happy.

Table of Contents

List of Tables

List of Figures

Abstract

Tectonic structures in structurally-complex areas play an important role in understanding the geology of the area. In this thesis, I concentrate on seismic attribute analysis and modeling of pop-up and graben structures in the Chicontepec Basin, Mexico. The Chicontepec play is characterized by thin turbidite and fan reservoirs that are separated by shales. Seismic attributes such as similarity and curvature provide a better understanding of the tectonic controls of the Chicontepec field. These attributes allow us to map faults, folds, pop-up and graben structures in the area. One major challenge in the Chicontepec area is the existence of igneous bodies. Shallow volcanic bodies affect the data negatively by giving rise to low-amplitude chaotic zones. To delineate these incoherent and chaotic zones and to provide a measure of confidence in the horizon picks, I compute disorder attribute throughout the survey.

Seismic modeling of the pop-up and graben structures provides a better understanding of the complex structures in the Chicontepec area. In this study, I compute a suite of wave-equation synthetic seismic models of the pop-up and graben structures in the area. Then, I apply seismic attributes to these models, and compare the results with those from the real data.

To improve data quality and condition the data for prestack inversion, I perform detailed velocity analysis, MPNMO correction, and prestack structure oriented filter on the prestack seismic data. Significant frequency enhancement and improved resolution are obtained after preconditioning seismic gathers. Simultaneous prestack inversion ties the wells and provides good resolution of the thin-bedded turbidites in the Chicontepec Basin, as well as potential future targets in the Mesozoic section.

Chapter 1: Introduction

Chicontepec Basin, discovered in 1925, is one of the most productive basins in Mexico. Commercial production in the basin began in 1952. Original oil in place is equal to 140 BBO, whereas only 0.1% of the OOIP (140 MBO) has been recovered yet. The basin is about 25 km wide (E-W), and 123 km long (N-S) (Abbaszadeh et al., 2008). The Chicontepec play is characterized by thin turbidite and fan reservoirs that are surrounded by shales. These sand reservoirs have very low porosity and permeability. In addition, they are occasionally multi-storied, and cut by mass transport complexes and mud slumps (Pena, 2010). The Chicontepec turbidite reservoirs have been altered by complex diagenetic processes, including extensive cementation. Since these reservoirs are tight, and have low porosity and permeability, the modern wells need to be hydraulically fractured in order to produce hydrocarbons from these reservoirs (Sarkar, 2011).

Seismic attributes such as similarity and curvature provide a better understanding of the tectonic controls of the Chicontepec field. These attributes allow us to map faults, fractures, collapse features, channels, folds, pop-up structures, horst and graben structures, and other geologic features. Murray (1968) correlated curvature to fracture enhanced production. McQuillan (1974) correlated fracture patterns to basement-controlled lineaments. Lisle (1994) correlated curvature computed from an outcrop to fracture density. Stewart and Wynn (2000) showed the value of computing curvature at multiple scales. Al-Dossary and Marfurt (2006) expanded these ideas to volumetric computations.

Diaz (2008) generated a chronostratigraphic model of the Chicontepec area, and defined the complex stratigraphic architecture of the area. Mai (2010) described lateral relationships between coherence and curvature, in order to give a better understanding of the complex geology of the Chicontepec Basin. Pena (2010) used coherence and curvature attributes to map igneous bodies in the Chicontepec Basin. Sarkar (2011) characterized foredeep turbidites in the northern Chicontepec Basin.

Objective of thesis

The primary objective of this thesis is to show how seismic attributes can be used to give a better understanding of tectonic environment of an area. The study focuses on a structurally-complex 3D seismic survey "Amatitlán" acquired in 2003 on the northern part of the Chicontepec Basin, Mexico. The second objective is to illuminate complex structures of the area, such as pop-up structures, using seismic modeling, and compare the results with those from the real data to test the accuracy of the interpretation. The final objective is to improve the data quality, especially in the deeper parts of the survey area, with detailed velocity analysis, NMO correction, and prestack structure oriented filtering.

Data available

Petróleos Mexicanos (Pemex), the Mexican state-owned petroleum company, headquartered in Mexico City, has provided me with a high-quality 3D prestack time migrated seismic survey (Amatitlán) acquired over the northern part of the Chicontepec Basin, Mexico (Figure 1.1). Table 1.1 summarizes some of the acquisition parameters of the Amatitlán survey.

The data were originally acquired and processed in 2003 by PEMEX Exploration and Production. However, acquisition obstacles such as human settlements, dense forest, and sensitive archeological sites gave rise to anomalies in the shallow section of the data. Therefore, to obtain better shallow imaging and to attenuate low frequency noise, the Amatitlán survey was reprocessed by PEMEX Exploration and Production in 2007. The following processing steps were applied before providing the data for this thesis:

- Careful deconvolution to detect and eliminate some of the reverberations, multiples and ghosts.
- Refraction statics to remove the irregular terrain effects on the data.
- Detailed velocity analysis to estimate the velocities properly.
- Coherent noise suppression to filter out coherent shot-generated noise.
- Trace mutes, datum corrections, aliased noise suppression, and azimuth moveout to condition the data for Kirchhoff prestack time migration.

Figure 1.2 shows the seismic fold map of the Amatitlán survey. The low fold areas are due to population centers, terrain effects, and swamps. Shallow volcanics exist in the area. Volcanic bodies give rise to reverberating refractions and interbed multiples on seismic data. Therefore, the igneous bodies affect the data negatively by giving rise to low-amplitude chaotic zones. Figure 1.3 is a representative vertical seismic profile from the Amatitlán survey that illuminates the data quality. The zones of poor data quality are due to shallow volcanic bodies and low fold areas. In addition, well log information is available from 324 wells in the eastern part of the northern Chicontepec Basin (Figure 1.4). However, almost all of these wells only penetrate to the Eocene objective at 700

ms, and most of them terminate on top of faults, unconformities, and horizontal layers. This means we don't have well control in the deeper section where the seismic data are of good quality.

Methodology

The methodology that I have used in my thesis work is summarized in Figure 1.5. I begin with seismic interpretation of the post stack data, picking faults and horizons of interest. Next, I use AASPI software to compute volumetric seismic attributes such as dip and azimuth, coherence and curvature to better delineate geologic features such as faults, graben structures, and pop-up structures in the study area. I compute a suite of wave-equation synthetic seismic models of the pop-up and graben structures in the area using vertical sections from the real data and well log information. Next, I apply seismic attributes to these models, and compare the results with those from the real data. With the prestack data, I perform detailed velocity analysis, MPNMO correction, and prestack structure oriented filter to improve the data quality. Then I tie the wells to seismic, and after well-seismic tie, using the density and sonic logs, I perform impedance inversion to map thin-bedded Chicontepec turbidites. Finally, I compare and integrate the results to better understand the geology of the area.

Thesis significance

The integration of seismic attributes, seismic modeling, data reprocessing, and impedance inversion will help better image and understand the geological structure of the Chicontepec area. In addition, this thesis quantifies which geologic features can be identified by a given seismic attribute.

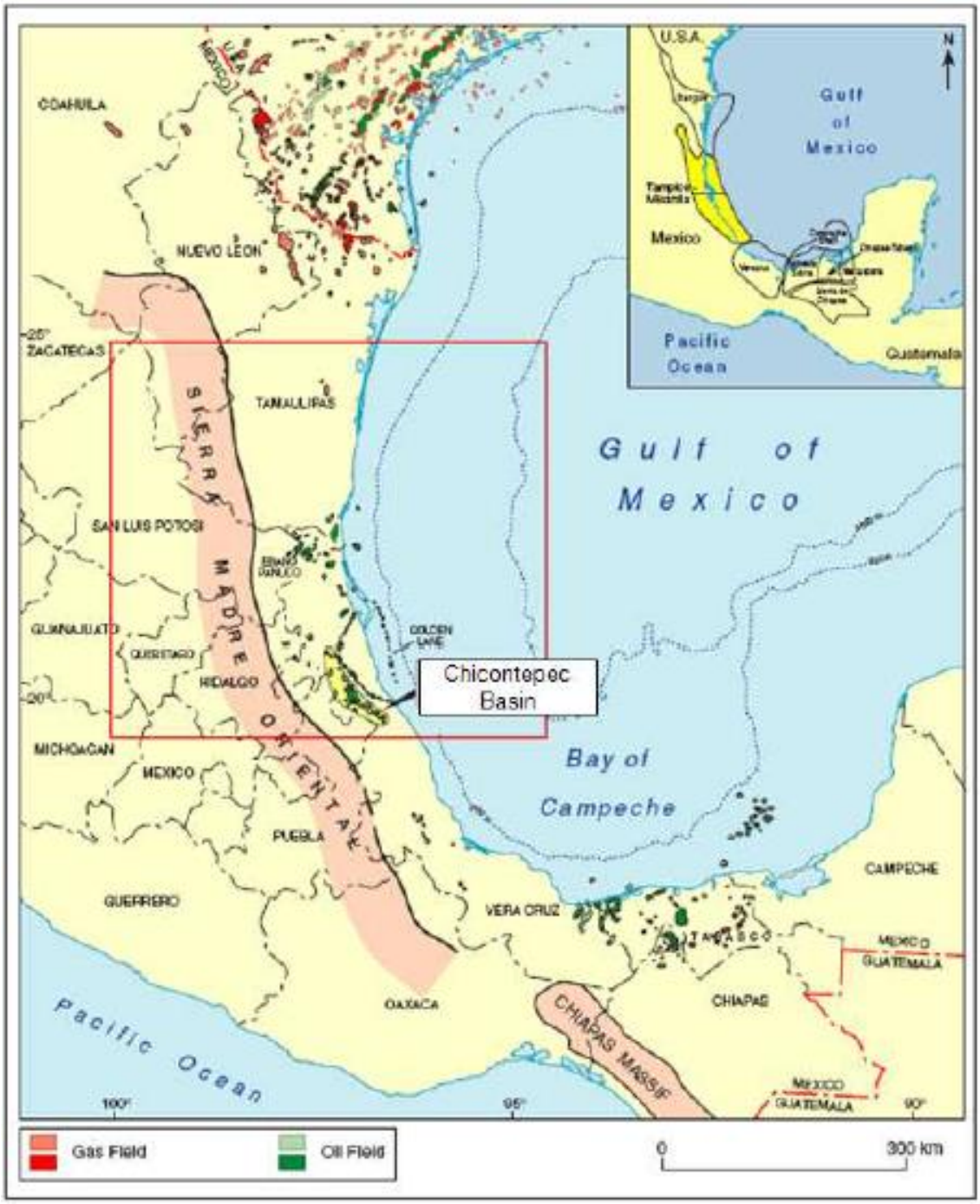

Figure 1.1. Location of Chicontepec Basin, Mexico (After Salvador, 1991).

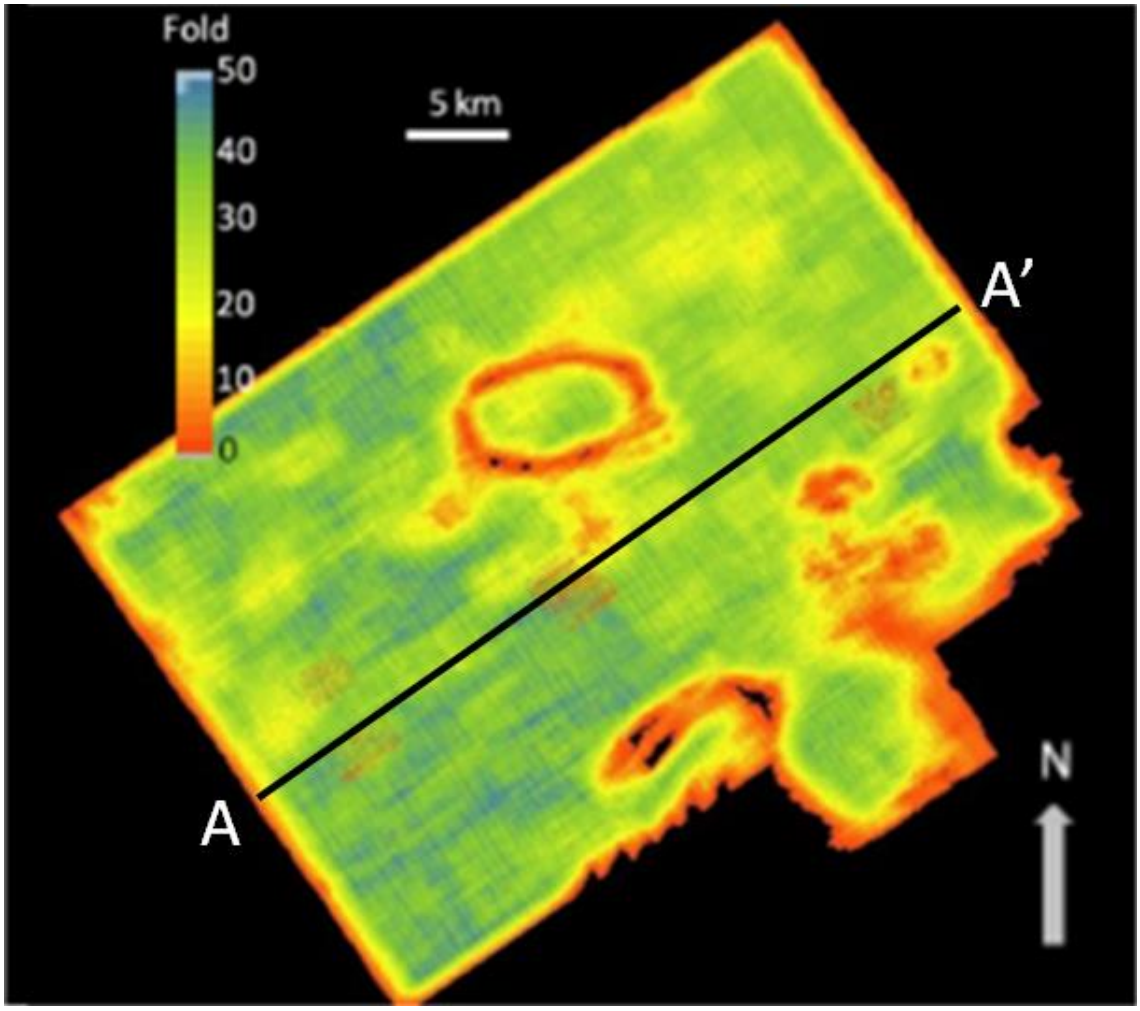

Figure 1.2. Seismic fold map of Amatitlán seismic survey (Modified from Pena, 2010).

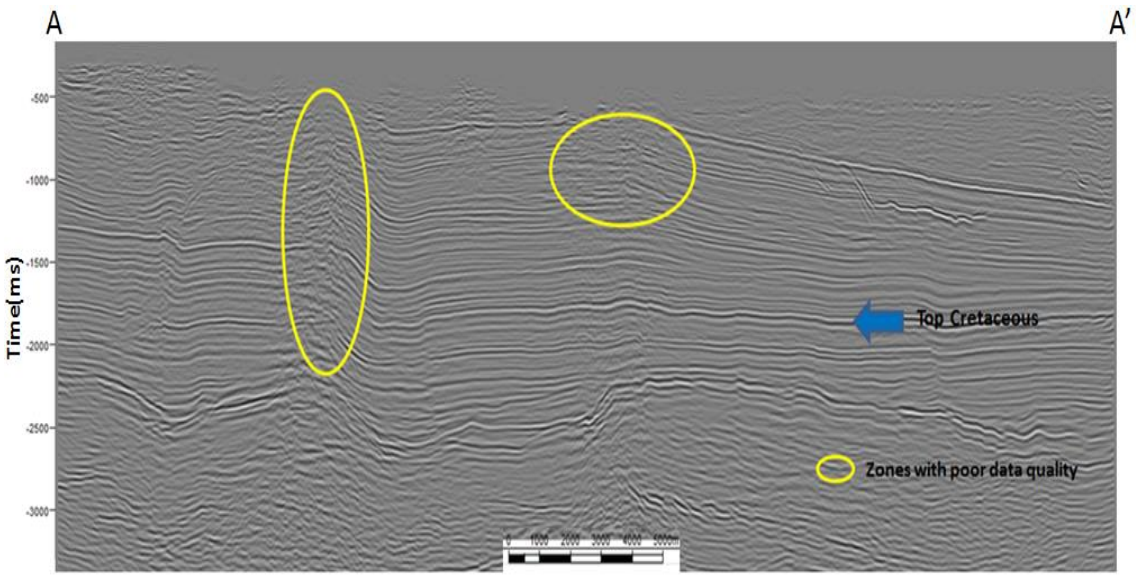

Figure 1.3. A representative vertical seismic section from the Amatitlán seismic survey. Location shown in Figure 1.2. Yellow ellipses represent zones with poor data quality due to shallow volcanic bodies and low fold zones.

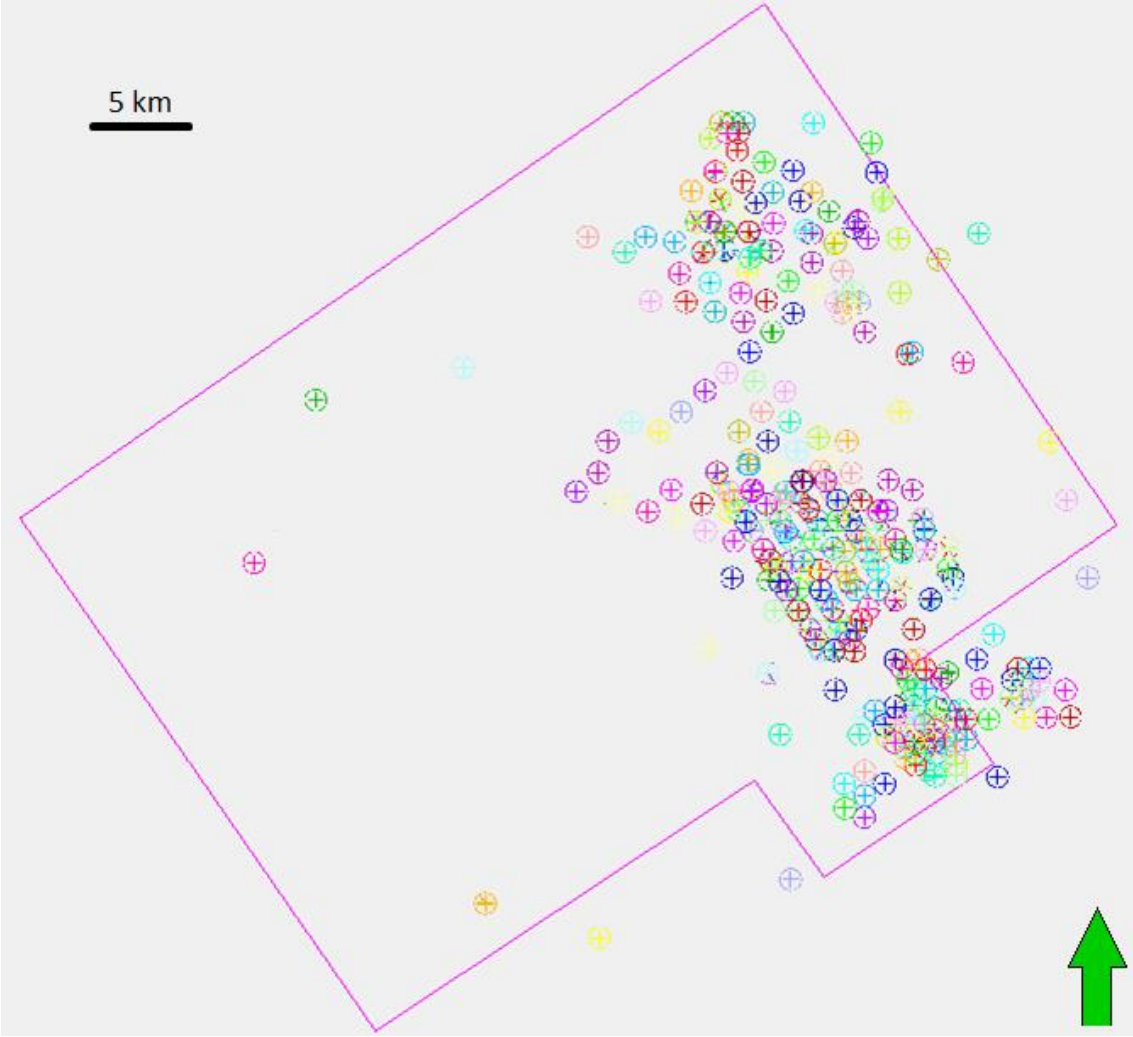

Figure 1.4. Location of the wells with well logs. Pink polygon demarcates the Amatitlán 3D seismic survey.

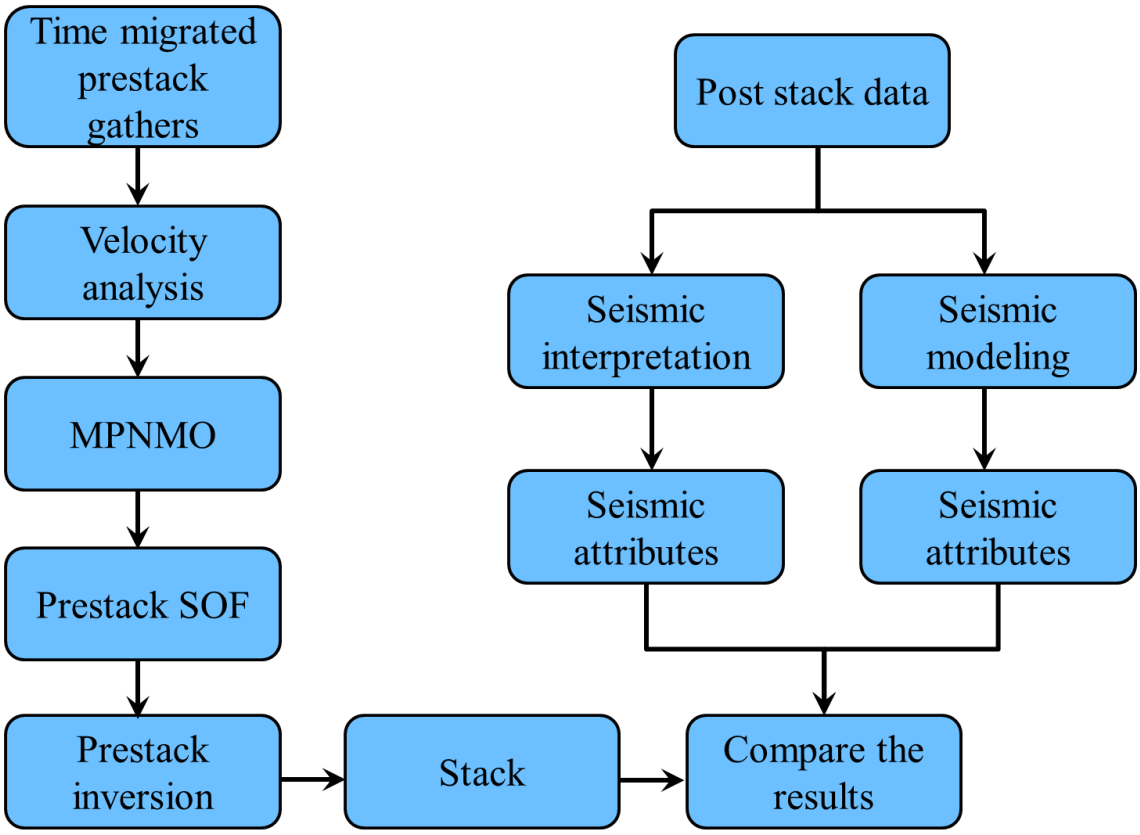

Figure 1.5. Seismic interpretation, modeling, and processing workflow.

Acquisition Parameters	
Source type	Dynamite
Bin size	25x25 m
Number of Inlines	1046
Number of Crosslines	1257
Receiver interval	50 m
Source interval	50 m
Receiver line interval	250 m
Source line interval	350 m
Recording time	6 s
Sample interval	4 ms

Table 1.1. Amatitlán seismic survey acquisition parameters.

Chapter 2: Geological Background

The Sierra Madre Oriental, formed during the Late Cretaceous-Early Tertiary Laramide Orogeny, is one of the major fold and thrust belts in Mexico (Morán-Zenteno, 1994). The Paleogene Chicontepec Formation, located in the Mexican part of the Gulf of Mexico, was deposited between the Sierra Madre Oriental and the Tuxpan Platform (Figure 2.1). Figure 2.2 indicates the schematic diagram of the Chicontepec foredeep, forming an accommodation zone between Sierra Madre Oriental and the Tuxpan Platform (Sarkar, 2011). The Chicontepec Formation, which is subdivided into three parts: lower, middle, and upper Chicontepec, is primarily composed of shales and thin-bedded sandstones (Bermúdez et al., 2006). The average thickness of the Chicontepec Formation in the study area is about 300-400 m, whereas the maximum thickness of the formation in the western Gulf of Mexico Tampico-Misantla Basin is about 2000 m (Bitter, 1993). The Chicontepec reservoir facies are highly compartmentalized and have very low porosity (1%-10%) and permeability (0.01-5 mD) (Bermudez et al., 2006).

The Chicontepec Basin is a subbasin of the Tampico-Misantla Basin located in the East Central Mexico. The tectonic evolution of the Tampico-Misantla Basin can be divided into four main stages: (1) Late Triassic-Callovian rifting, graben development, and opening of the Gulf of Mexico; (2) Late Jurassic-Early Cretaceous drift stage, development of passive margin, and widespread marine transgression; (3) Late Cretaceous marine connection of the Gulf of Mexico Basin to the Pacific Ocean; and (4) Late Cretaceous-Early Tertiary Laramide Orogeny; uplift of the Sierra Madre Oriental in eastern Mexico and the Sierra Madre de Chiapas in southeastern Mexico, and

associated foredeep development (Morán-Zenteno, 1994; Cantú-Chapa, 2001; Goldhammer and Johnson, 2001; Diaz, 2008).

During the Triassic-Jurassic graben development, first the volcanic deposits, and then during Middle Jurassic the extensive salt deposits were accumulated in the Gulf of Mexico (Diaz, 2008). The Late Jurassic-Early Cretaceous passive margin development and marine transgression led the seawater to enter the basin from the Pacific Ocean across central Mexico, and a large inland sea was developed. Taman and San Andrés shales and carbonates were deposited during this time in the Tampico-Misantla Basin (Salvador, 1991; Goldhammer and Johnson, 2001; Diaz, 2008). During the Late Paleocene-Early Eocene, partly turbiditic, and fine-grained clastic sediments of the Chicontepec Formation were deposited in submarine canyons within the east-migrating foredeep (Diaz, 2008). During the Oligocene, the coarse-grained nonmarine and shallow marine clastics (Palma Real and Meson Formations) and marine shales (Horcones and Alazan Formations) were deposited. Clastic shelf systems were swiftly formed and were strongly progradational across the whole basin (Horbury et al., 2003; Diaz, 2008). Paleocene consists of the formations Velazco, Lower Chicontepec and Middle Chicontepec. The Lower Eocene section is composed of the formations Aragon and Upper Chicontepec Channel. In addition, the Guayabal Formation was deposited in the Middle Eocene and the Tantoyuca and Chapopote formations were deposited in the Upper Eocene (Figure 2.3).

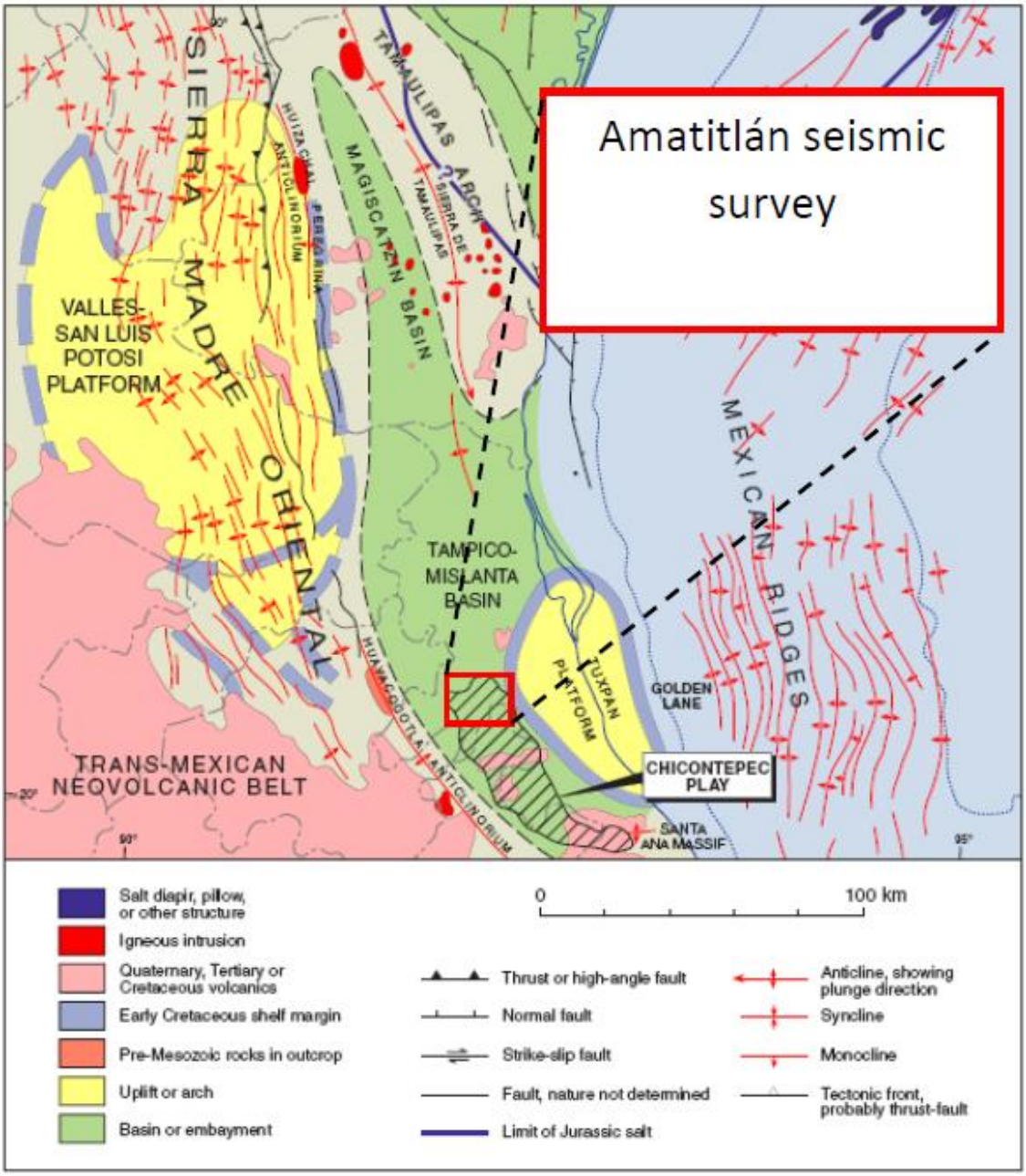

Figure 2.1. Regional structural setting of the Tampico-Misantla Basin, the Chicontepec Basin and the Amatitlán seismic survey (After Salvador 1991; Goldhammer and Johnson, 2001; Diaz, 2008; Pena, 2010).

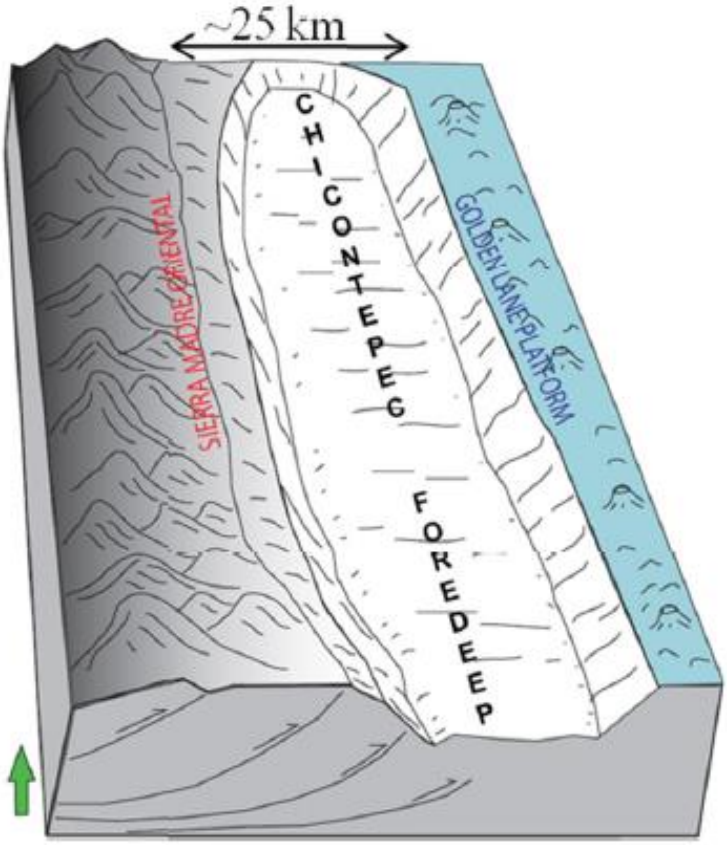

Figure 2.2. Schematic diagram showing the Chicontepec foredeep forming an elongated accommodation zone between Sierra Madre Oriental and Golden Lane (Tuxpan) Platform (After Sarkar, 2011).

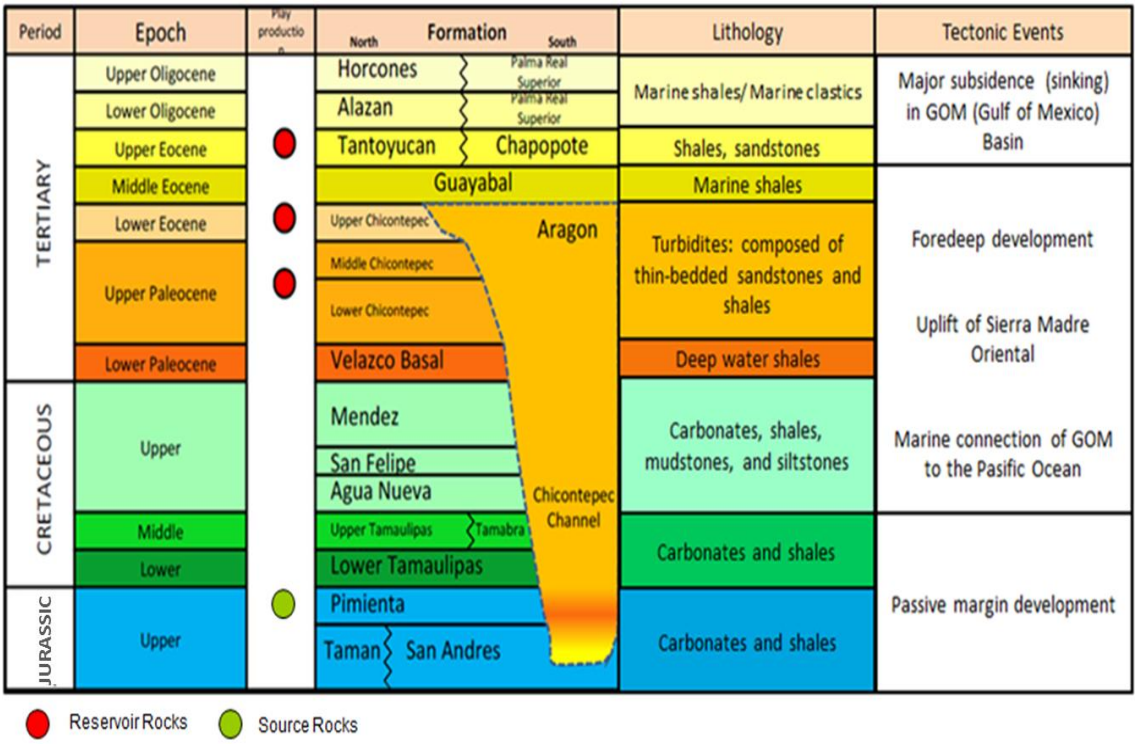

Figure 2.3. Regional stratigraphic column of the study area (Modified from Sarkar, 2011).

Chapter 3: Seismic Attributes Applied to Chicontepec Basin

A seismic attribute is any measure of seismic data that helps us interpret features of interest. Seismic attributes are a powerful tool for seismic interpretation allowing the geoscientist to interpret faults and channels, understand the depositional environment, and resolve the structural deformation history more rapidly. Seismic attributes such as similarity and volumetric curvature allow us to map structural features of interest. While similarity attributes measure lateral changes in the waveform and allow us to map reflector offsets, lateral changes in stratigraphy, and chaotic features; curvature attributes measure lateral changes in dip magnitude and dip azimuth, and therefore allow us to map folds, collapse features, and differential compaction. Both types of the attributes are widely used in fault detection, with each attribute having its advantages and disadvantages. For faults that have very small displacement, the reflectors appear to have a subtle change in dip, but not in waveform. Therefore, these faults may not be seen on coherence attribute volumes; whereas, these features appear as a slight flexure on curvature attribute volumes. Faults with no reflector rotation can be seen on coherence attribute volumes, whereas they may not appear on curvature attribute volumes. For faults with significant offset, curvature attributes are often laterally displaced from the fault trace because curvature attributes often track dip changes on either side of the fault (Chopra and Marfurt, 2007). A fault is commonly seen as a pattern on seismic attribute volumes. A low coherence anomaly appears on the fault plane, and curvature anomalies appear on either side of the fault. In this study, I use volumetric seismic attributes to identify faults, pop-up structures formed due to compression, and graben structures in the Chicontepec Basin.

Energy ratio similarity

Energy ratio similarity attribute is only sensitive to changes in waveform, and not changes in amplitude. The configuration includes KL-filtering a window of data, computing its energy, and finally normalizing by the energy of the unfiltered data (Chopra and Marfurt, 2007).

Figure 3.1 shows energy ratio similarity time slice in the deeper part of the survey. The low coherence chaotic zones are due to shallow volcanic bodies and low fold areas. The main faults and chaotic zones are well delineated on the energy ratio similarity time slice.

Sobel filter similarity

Introduced by Luo et al. (1996), Sobel filter similarity is an amplitude-sensitive, multitrace attribute. In contrast to the energy ratio similarity, Sobel filter similarity measures lateral changes in amplitude. There are three steps for computation of this attribute. Initially, derivatives along a plane defined by reflector dip and azimuth are taken. Next, to improve the signal-to-noise ratio, these derivatives are stacked along a vertical analysis window. Finally, the result is normalized by dividing the differences by the energy of the input traces, such that relative changes in amplitude are measured (Chopra and Marfurt, 2007).

Figure 3.2 shows Sobel filter similarity time slice. Similar to the energy ratio similarity attribute, faults and chaotic zones are well imaged on the Sobel filter similarity time slice. Subtle features below ¼ wavelength resolution with no significant change in waveform are better imaged by Sobel filter similarity attribute compared to the energy ratio similarity attribute. The reason for this is because Sobel filter similarity

is sensitive to changes in amplitude, not in waveform. Figure 3.3 shows top Jurassic level horizon slice through Sobel filter similarity attribute. There are some differences between similarity time slice and horizon slice. Most of the main faults seen on the horizon slice are correlated to the pop-up structures in the deeper part of the survey area. Pop-up structures are better delineated on the horizon slice, whereas chaotic zones are better delineated on the time slice. Main fault zones are well illuminated on both slices.

Disorder attribute

The original algorithm of the disorder attribute is based on cascading the second derivative in the x, y, and time direction on a window of the energy (or the power) of the data (Al-Dossary and Wang, 2013). This is identical to square the data and then to filter it with a symmetrical 3x3x3 operator:

$$\left\{\begin{bmatrix} 1 & -2 & 1 \\ -2 & 4 & -2 \\ 1 & -2 & 1 \end{bmatrix}, \begin{bmatrix} -2 & 4 & -2 \\ 4 & -8 & 4 \\ -2 & 4 & -2 \end{bmatrix}, \begin{bmatrix} 1 & -2 & 1 \\ -2 & 4 & -2 \\ 1 & -2 & 1 \end{bmatrix}\right\}$$

The disadvantage of this algorithm is that the algorithm is sensitive to local average amplitude. Low disorder values are obtained for chaotic zones with low amplitude, such as the ones that are affected by the shallow volcanic bodies in the Chicontepec Basin. Thus, Ha and Marfurt (2013) modified the algorithm, and they divided the attribute by the RMS amplitude of the windowed data (Ha and Marfurt, 2013). The modified disorder attribute can be used to predict horizon picking confidence.

Figure 3.4 shows a seismic amplitude vertical slice in the middle of the survey. While the seismic data are of good quality, some parts of the data have been severely affected due to presence of shallow igneous bodies. Volcanics give rise to backscattered noise, reverberating refractions, and interbed multiples on the seismic data. Therefore, they affect the data negatively by giving rise to low-amplitude chaotic zones. In these chaotic zones, it is harder to pick horizons on seismic amplitude sections. The disorder attribute can be used to provide a measure of confidence in the picks by delineating the incoherent and chaotic zones. Figure 3.5 shows a disorder vertical slice with the top Jurassic level horizon. In this figure, black indicates high disorder, which corresponds to chaotic zones with poor data quality. In contrast, white indicates low disorder, which corresponds to high quality zones.

After horizon picking, the disorder attribute can be used to quality control the picks. The time-structure map of the top Jurassic horizon is shown in Figure 3.6. The disorder attribute extracted along the top Jurassic horizon is shown in Figure 3.7. The smaller the values on the disorder horizon slice, the more confident we are of our picks. Figure 3.8 shows a disorder time slice at the approximate top Jurassic level. Compared to the disorder horizon slice, more poor data quality, high disorder zones can be identified on the time slice. This reveals the quality and confidence of the horizon picks. While the disorder attribute is insensitive to faults and structure, it correctly represents the horizon-picking confidence and delineates chaotic zones.

Curvature

Curvature in two dimensions is defined by Chopra and Marfurt (2007) as the reciprocal of the radius of a circle tangent to a curve at a particular point (Figure 3.9).

Anticlinal features have positive curvature, synclinal features have negative curvature, and planar features have zero curvature. Portions with a constant dip have zero curvature as well (Chopra and Marfurt, 2007).

In three dimensions, curvature at a point is defined by fitting two circles within orthogonal planes tangent to a surface at the analysis point (Figure 3.10). The orthogonal planes are rotated until we find the circle with the minimum radius. The reciprocal of the radius of this circle is defined as the maximum curvature, k_{max}. The second tangent circle perpendicular to the first circle with the minimum radius will contain the maximum radius. The reciprocal of the radius of this circle is defined as the minimum curvature, k_{min}. Minimum and maximum curvatures, k_{min} and k_{max} can be expressed in terms of the most-positive and most-negative principal curvatures, k_1 and k_2, where $k_{max} = \text{MAX}(|k_1|, |k_2|)$ and $k_{min} = \text{MIN}(|k_1|, |k_2|)$ (Chopra and Marfurt, 2007). Figure 3.11 shows a cartoon of a fold where positive curvature anomalies are observed along the anticlinal fold axis, and negative curvature anomalies are observed along the synclinal fold axis. Compared to k_{pos} and k_{neg} anomalies, k_1 and k_2 anomalies are correlated to the more geologically relevant anticlinal and synclinal fold axes (Mai, 2010).

For this work, the most-positive and most-negative principal curvatures, k_1 and k_2 provided better images of the faults, pop-up structures and graben structures in the Chicontepec area. Figure 3.12 shows a time slice through the most-positive principal curvature and the most-negative principal curvature. Compared to the similarity attributes, all the main faults and deformation zones are better illuminated on the curvature time slice. Faults on the curvature time slice appear to be more continuous

than faults on the similarity time slices. In addition, curvature leads us to identify subtle faults that are not seen on similarity volumes. The reason for this is because curvature attributes measure changes in dip magnitude and dip azimuth, while similarity attributes measure changes in the waveform. For faults with very small displacement, the reflectors appear to have a subtle change in dip, but not in waveform. Therefore, these faults can be seen on curvature volume, but not on coherence. Figures 3.13 and 3.14 show k_1 and k_2 attributes extracted along top Jurassic level horizon. Both attributes provide good images of the anticlinal and synclinal features, faults and the pop-up structures on the horizon slices. Upthrown blocks of the faults give rise to positive curvature anomalies, while downthrown blocks are imaged as negative curvature anomalies. Compared to the curvature time slice, pop-up structures are much better imaged on the curvature horizon slices. On the other hand, faults are much better imaged on the curvature time slice. Figures 3.15 and 3.16 show uninterpreted and interpreted vertical slices illuminating the pop-up structures, main faults, and horizons of interest in the area. Significant competency contrast between the units plays an important role in formation of these pop-up structures. The incompetent basal layer, mostly composed of shale, is overlain by competent units, composed of carbonates and sandstones. There are two thrust faults on both limbs of the pop-up structures. One of these two faults terminates against the other.

The appearance of a pop-up structure

Figure 3.17a shows an interpreted vertical seismic amplitude section of a pop-up structure in the western part of the survey. The structure is deformed due to compression, forming a symmetrical pop-up block in the middle, and two reverse faults

on both limbs. These faults are formed at the most sheared parts of the structure. The pop-up structure is not perfectly symmetric. The reason for this is because one limb is rotated more than the other limb. Figure 3.17b shows Sobel filter similarity vertical slice. The two reverse faults are successfully imaged as low similarity anomalies on this vertical slice. Blended image of the most-positive principal curvature, k_1, the most-negative principal curvature, k_2, and seismic amplitude is shown in Figure 3.17c. For both faults, positive curvature anomalies are observed (in red) on the hanging wall blocks, whereas negative curvature anomalies are observed (in blue) on the footwall blocks. All vertical slices are plotted with no vertical exaggeration for a more accurate interpretation. We observed that co-rendering two attributes works best when one image is plotted against gray scale and the other image is plotted against a polychromatic color bar.

The appearance of a graben structure

Figure 3.18a shows an interpreted vertical seismic amplitude section of a graben structure in the northeastern part of the survey. The structure is formed due to extension, forming a graben block in the middle that has dropped due to normal faulting on either side. Figure 3.18b shows Sobel filter similarity vertical slice. The two normal faults can be identified as low coherence anomalies on this vertical slice. These faults are smaller when compared to the faults on Figure 3.17b. Figure 3.18c shows blended image of the most-positive principal curvature, k_1, the most-negative principal curvature, k_2, and seismic amplitude. In contrast to the pop-up structure; for both normal faults, negative curvature anomalies are observed (in blue) on the hanging wall blocks, whereas positive

curvature anomalies are observed (in red) on the footwall blocks. All vertical slices are plotted with no vertical exaggeration.

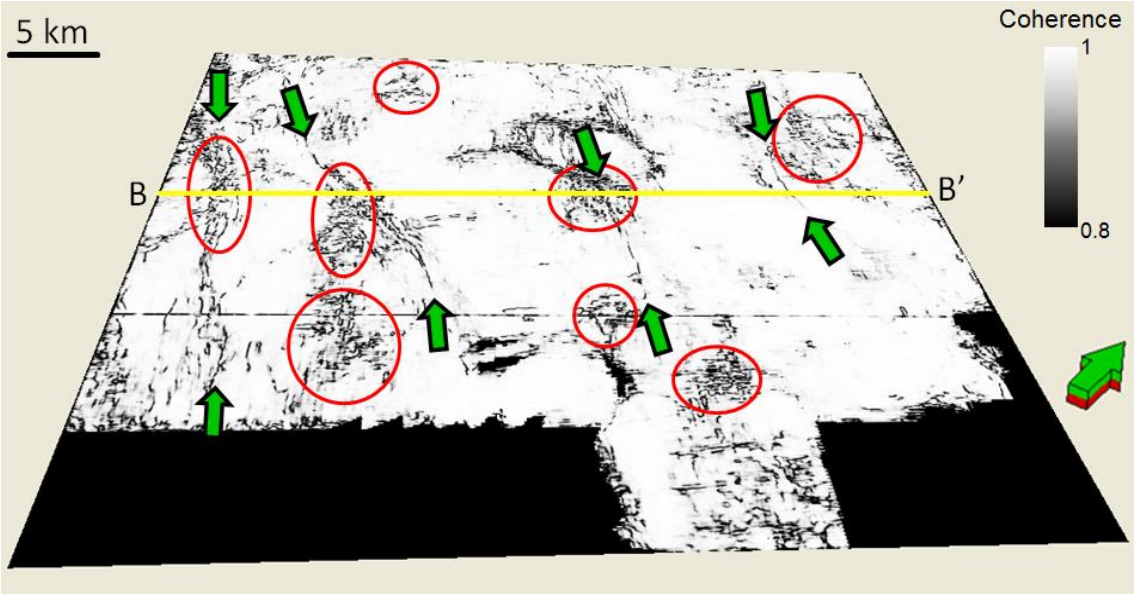

Figure 3.1. Energy ratio similarity time slice at t=1800 ms at the approximate top Jurassic level. Line B-B' indicates the position of the vertical slice shown in Figure 3.4. The low similarity chaotic zones (in black color) due to shallow volcanic bodies are indicated by red circles. Green arrows indicate main fault zones in the study area. Note all faults and chaotic zones are well mapped on the energy ratio similarity time slice.

Figure 3.2. Sobel filter similarity time slice at t=1800 ms at the approximate top Jurassic level. The low similarity chaotic zones (in black color) due to shallow volcanic bodies are indicated by red circles. Green arrows show main fault zones in the study area. Similar to the energy ratio similarity time slice, all faults and chaotic zones with poor data quality are well imaged on the Sobel filter similarity time slice.

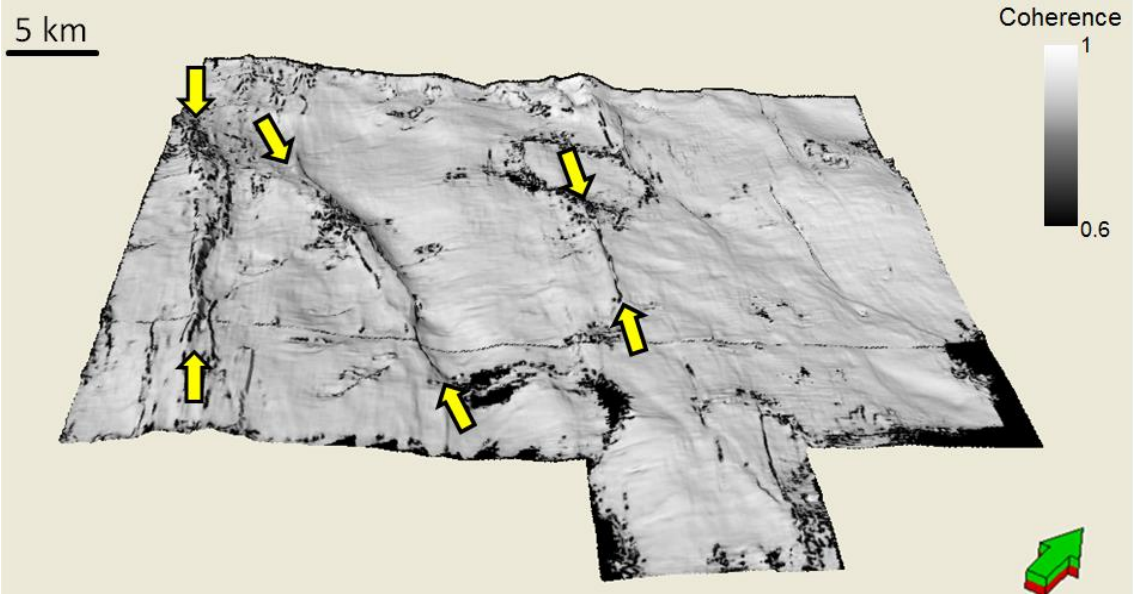

Figure 3.3. Sobel filter similarity horizon slice extracted along the top Jurassic level horizon. Yellow arrows indicate the main faulted pop-up structures in the deeper part of the survey. Most of the main fault zones are correlated to the pop-up structures in the area. Compared to the Sobel filter similarity time slice shown in Figure 3.2, pop-up structures are better illuminated on the horizon slice. On the other hand, chaotic zones are better imaged on the time slice. Main fault zones are well imaged on both slices.

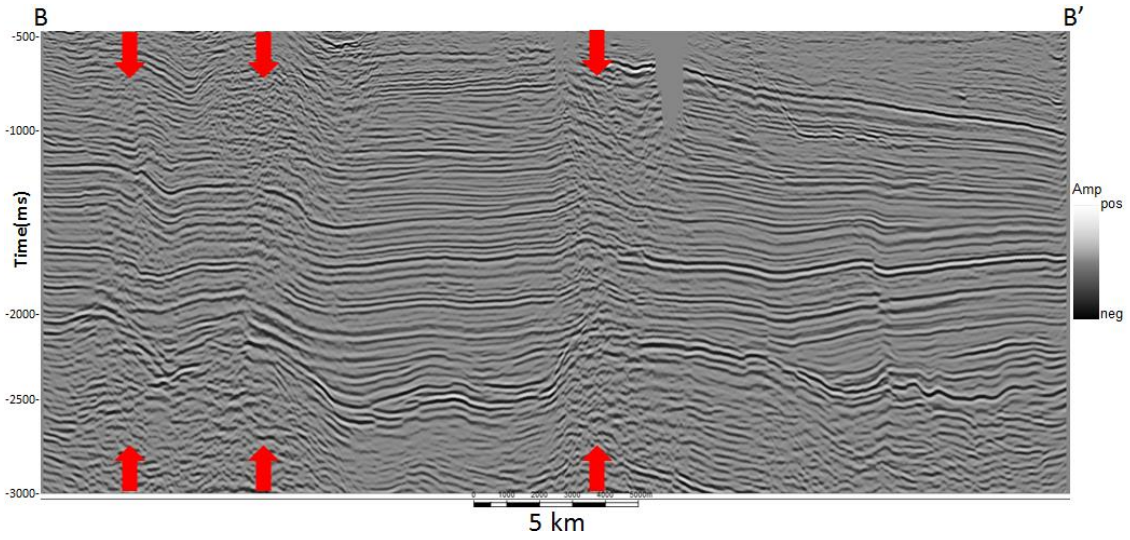

Figure 3.4. Seismic amplitude vertical slice B-B'. Location shown in Figure 3.1. Red arrows indicate incoherent chaotic zones due to shallow volcanic bodies. These chaotic zones affect the data quality negatively.

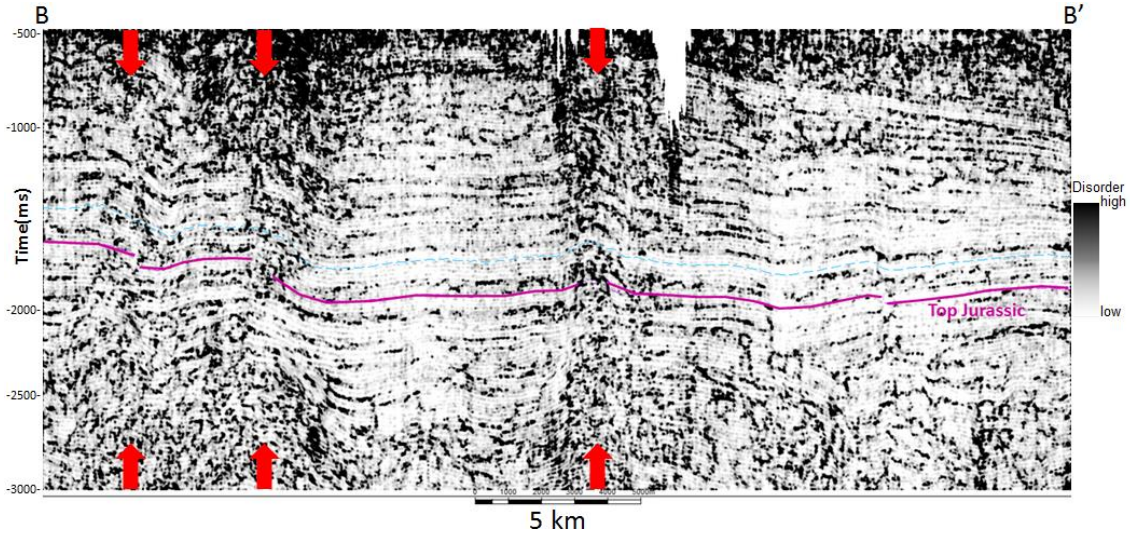

Figure 3.5. Disorder vertical slice B-B'. Location shown in Figure 3.1. Red arrows indicate incoherent chaotic zones due to shallow volcanic bodies. Note that chaotic zones give rise to high disorder (black color). These are the zones with poor data quality. Magenta color picked horizon shows top Jurassic level horizon shown in Figure 3.6. Note that low disorder (white color) shows high quality areas. These are the zones where our picks will be easier to make and where our horizons will be more accurate.

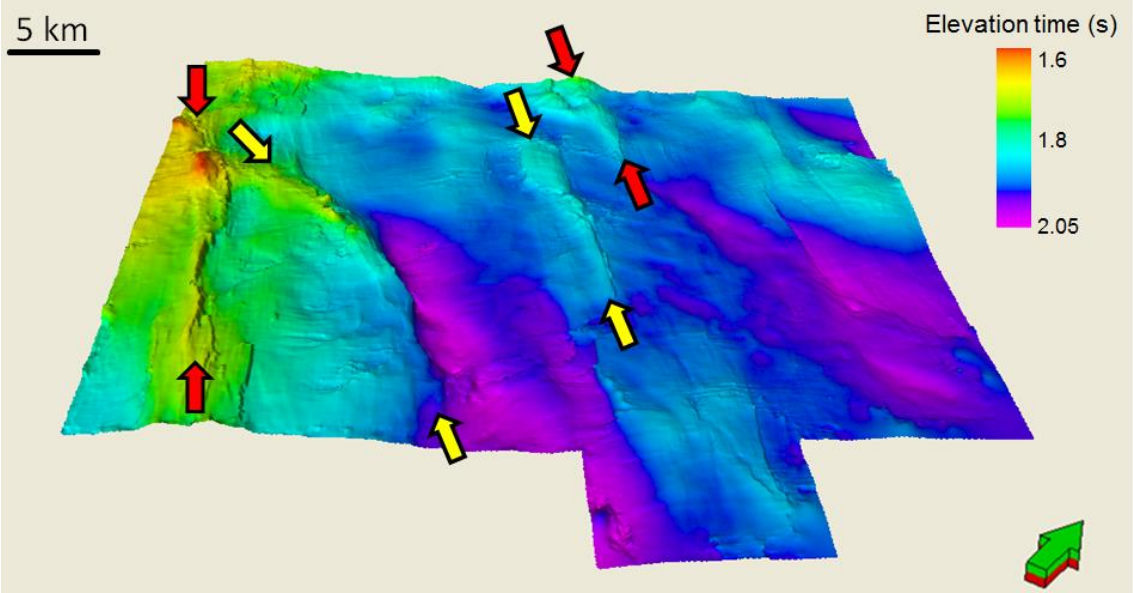

Figure 3.6. Time-structure map of the top Jurassic level horizon. Red and yellow arrows show the main pop-up structures in the study area. Note that all the pop-up features are well illuminated and can be easily identified on the time-structure map.

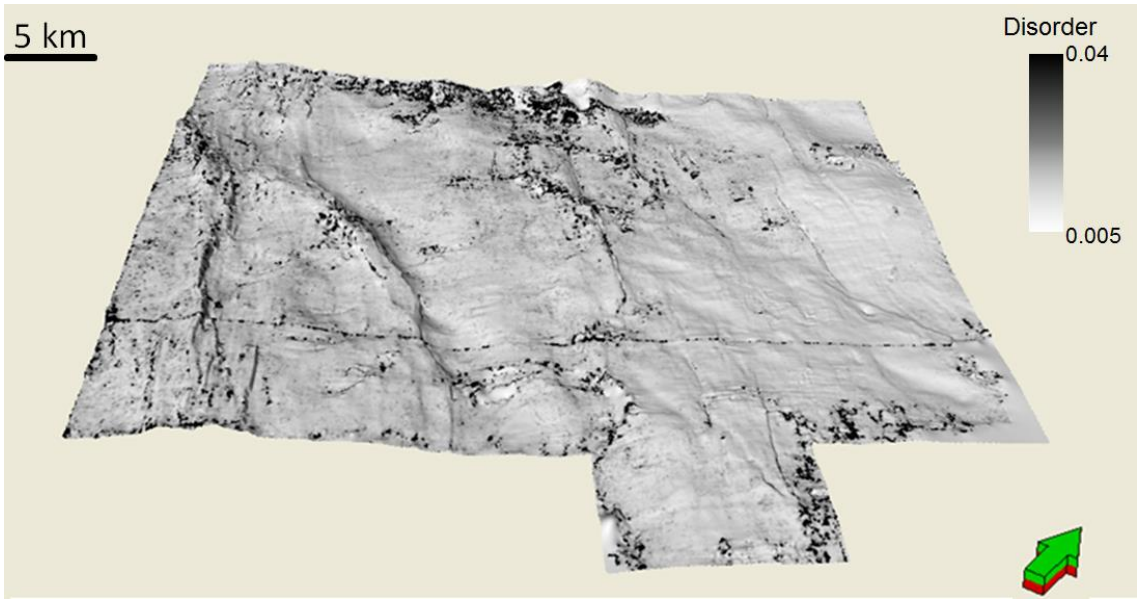

Figure 3.7. Disorder attribute horizon slice extracted along the top Jurassic level horizon. High disorder (black color) represents zones with poor data quality where we are not confident from our picks. Low disorder (gray and white colors) shows zones with high data quality where we are confident from our horizon picks. Since we don't have much high disorder zones along the top Jurassic level horizon, it can be said that our picks are quite accurate.

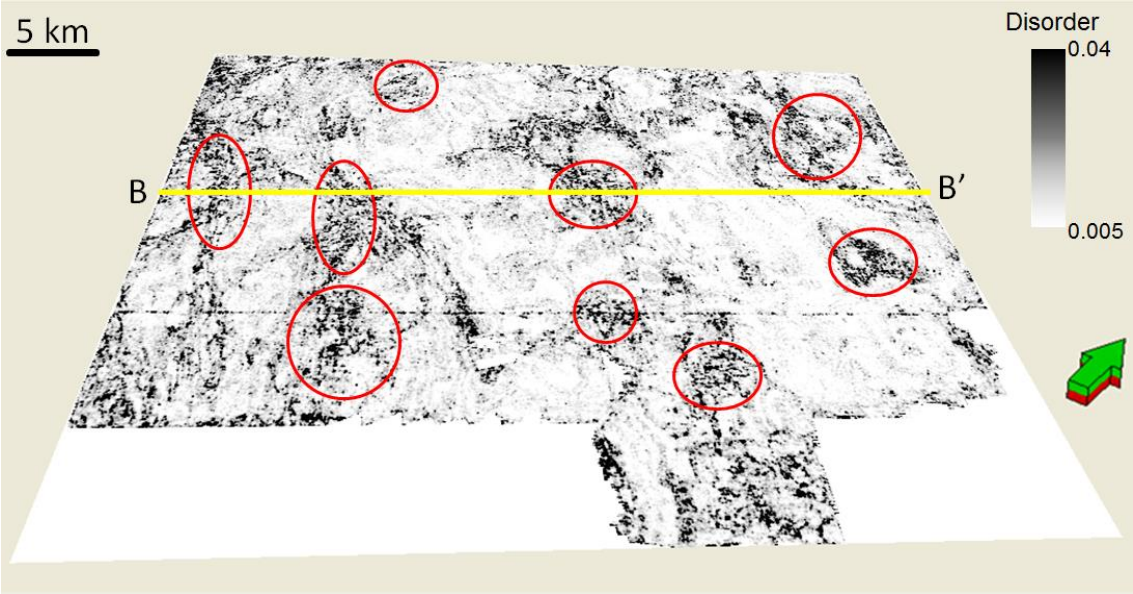

Figure 3.8. Disorder attribute time slice at t=1800 ms at the approximate top Jurassic level. The high disorder chaotic zones (in black color) due to shallow volcanic bodies are indicated by red circles. Compared to the previously shown horizon slice, more chaotic high disorder zones (black color) are observed. This occurs because I have picked a high amplitude, and thus high signal-to-noise ratio horizon. The time slice cuts through both high and low signal-to-noise ratio reflectors. Chaotic zones are well imaged on the disorder time slice, whereas faults are not well delineated because the disorder attribute is designed to be insensitive to faults, channels and other lineaments.

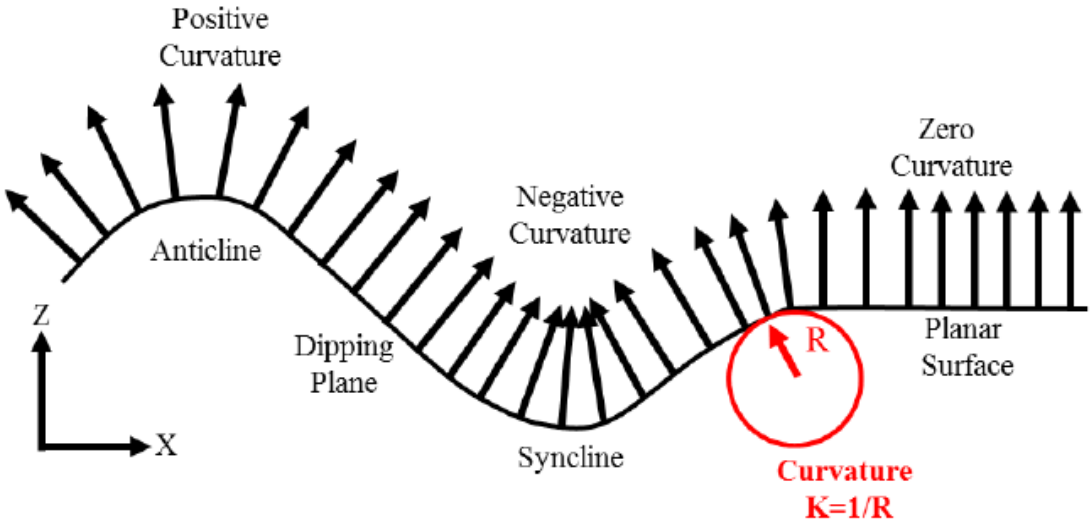

Figure 3.9. An illustrated definition of 2D curvature. Anticlinal features have positive curvature, synclinal features have negative curvature, and planar features have zero curvature (After Roberts, 2001).

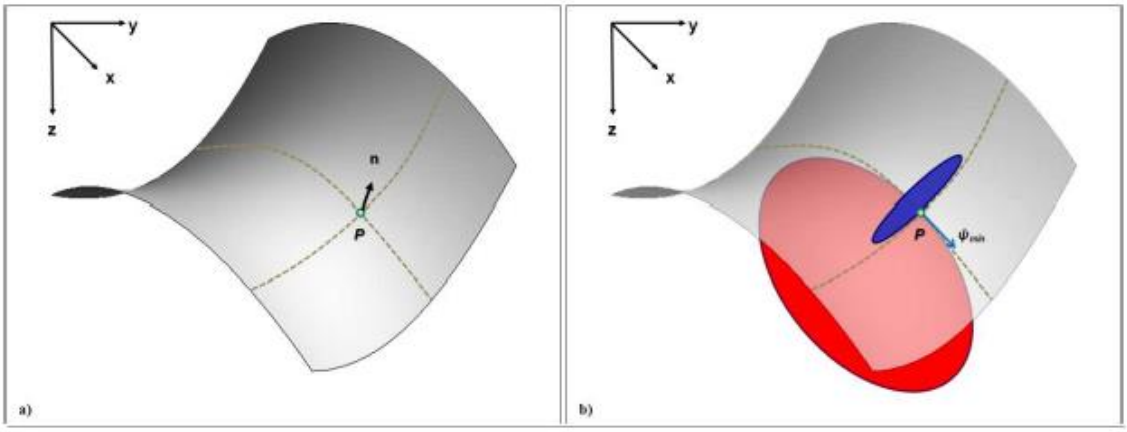

Figure 3.10. (a) A quadratic surface with the normal, n, defined at point *P*. (b) The circle tangent to the surface with minimum radius defines the magnitude of the maximum curvature, $|k_{max}| \equiv 1/R_{min}$ (in blue). For a quadratic surface, the plane perpendicular to that containing the previously defined blue circle will contain one whose radius is maximum, which defines the magnitude of the minimum curvature, $|k_{min}| \equiv 1/R_{max}$ (in red). Anticlinal features have positive values of k_{max}, and synclinal features have negative values of k_{max} (After Mai, 2010).

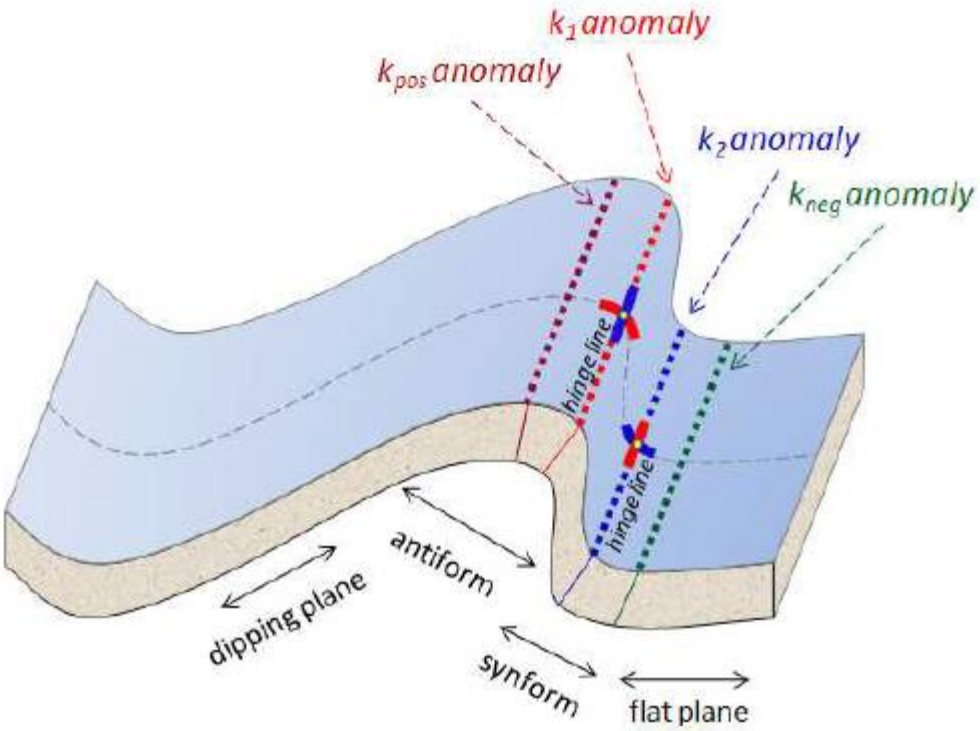

Figure 3.11. Lateral displacement of positive (k_{pos}) and negative curvature (k_{neg}) anomalies, correlating to the crest and trough of the folded structure. The most-positive and most-negative principal curvature anomalies (k_1 and k_2), correlating to the more geologically relevant anticlinal and synclinal fold axes (After Mai, 2010).

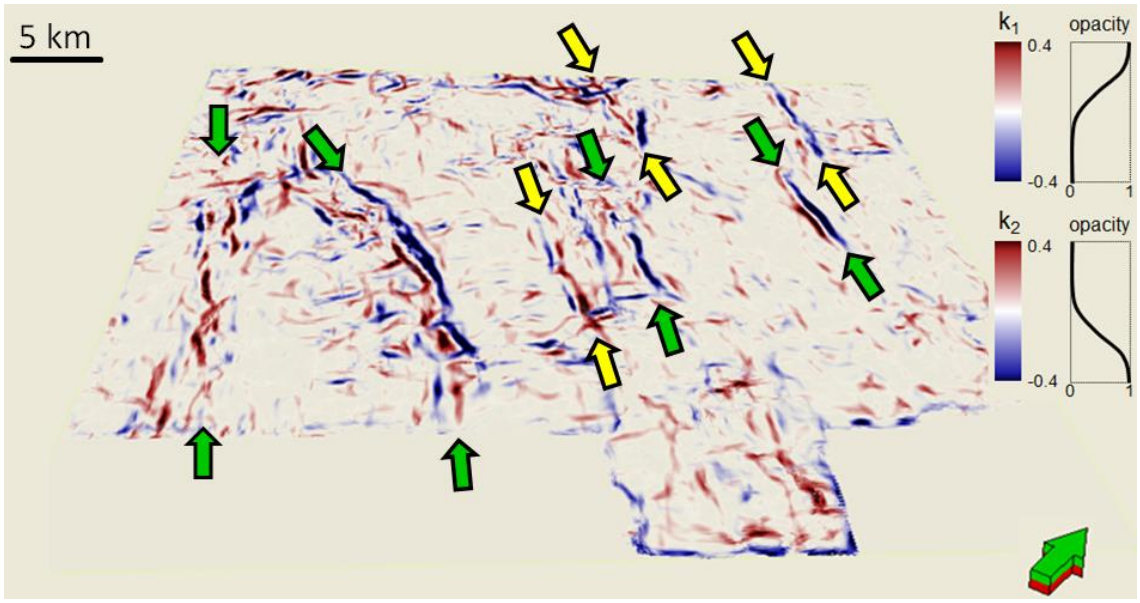

Figure 3.12. The most-positive principal curvature and the most-negative principal curvature time slice at t=1800 ms at the approximate top Jurassic level. Green arrows indicate the main fault zones both seen on curvature and coherence time slices. Yellow arrows indicate faults seen on curvature, but not on coherence. Note that compared to the similarity time slices, the main fault zones, as well as smaller scale faults are much better imaged on the curvature time slice.

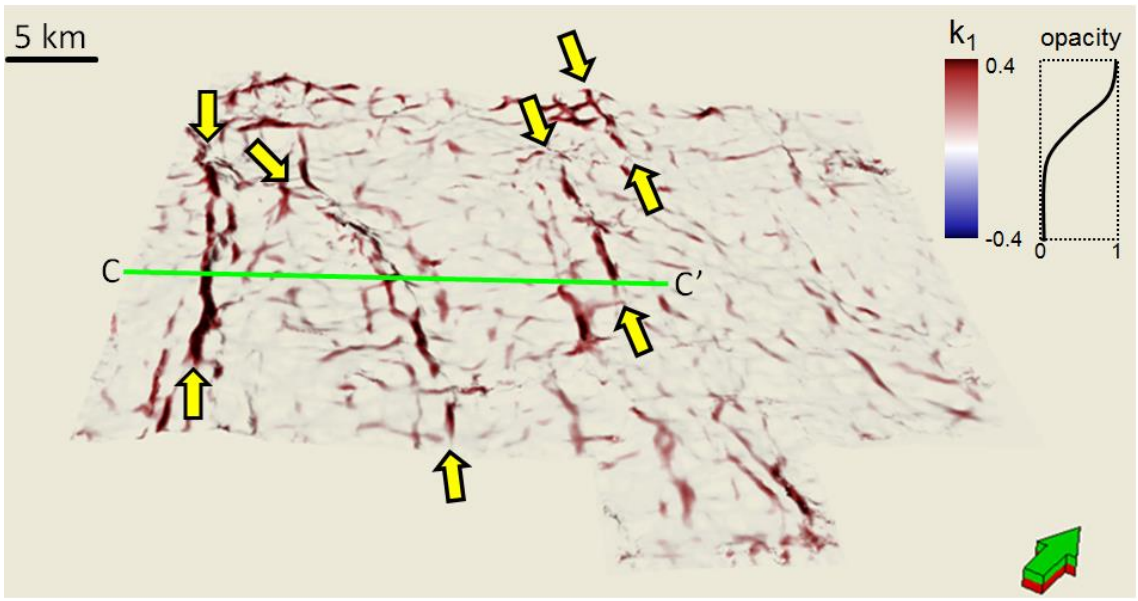

Figure 3.13. The most-positive principal curvature horizon slice extracted along the top Jurassic level horizon. The green line indicates the position of the vertical slice shown in Figures 3.15 and 3.16. The yellow arrows indicate the main faulted pop-up structures in the survey area. Positive curvature anomalies (in red) are observed on the pop-up blocks. Note that compared to the curvature time slice, the pop-up structures are much better imaged on the most-positive principal curvature horizon slice.

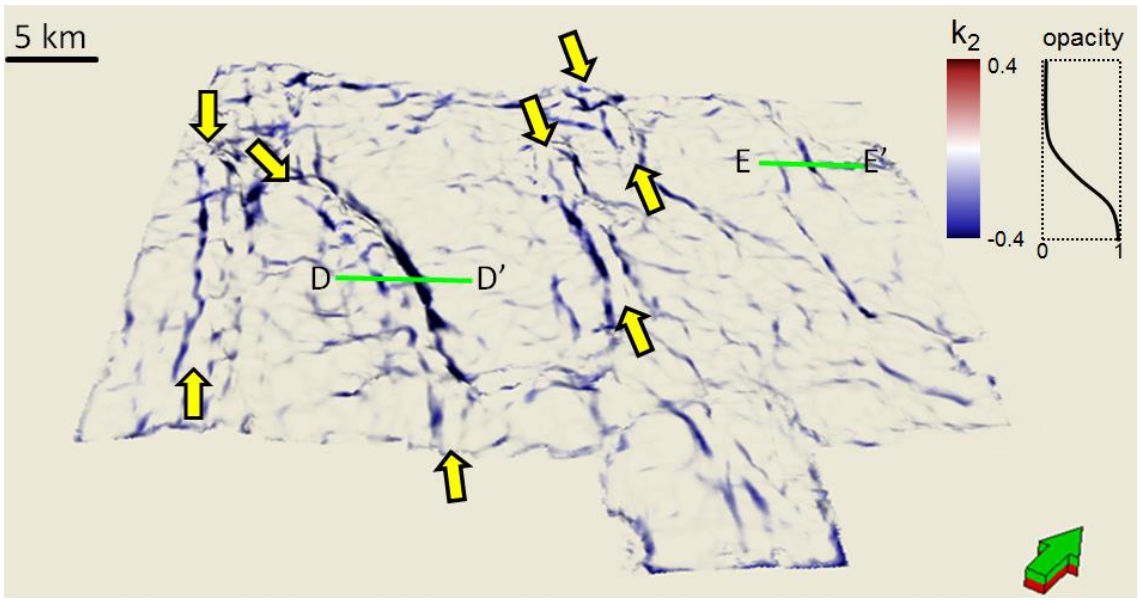

Figure 3.14. The most-negative principal curvature horizon slice extracted along the top Jurassic level horizon. The green lines indicate the positions of the vertical slices shown in Figures 3.17 and 3.18. The yellow arrows indicate the main faulted pop-up structures in the survey area. No negative curvature anomalies are observed on the pop-up blocks. In contrast, negative curvature anomalies (in blue) are observed on the downthrown blocks of the faults and on either side of the pop-up blocks. Note that compared to the curvature time slice, the pop-up structures are much better imaged on the most-negative principal curvature horizon slice.

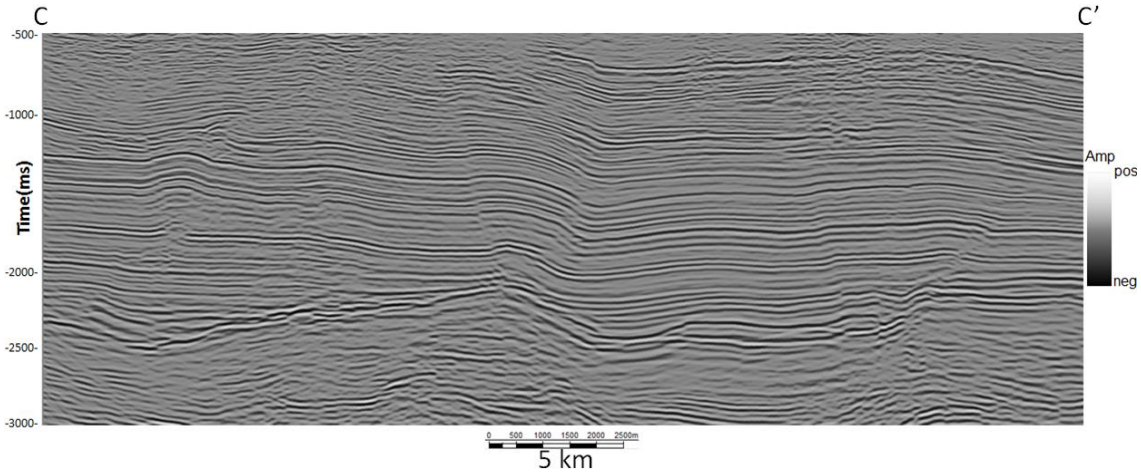

Figure 3.15. Uninterpreted seismic amplitude vertical slice C-C' shown in Figure 3.13. Note that the vertical slice cuts through three faulted pop-up structures shown in Figure 3.13. The figure is plotted with vertical exaggeration 3:1.

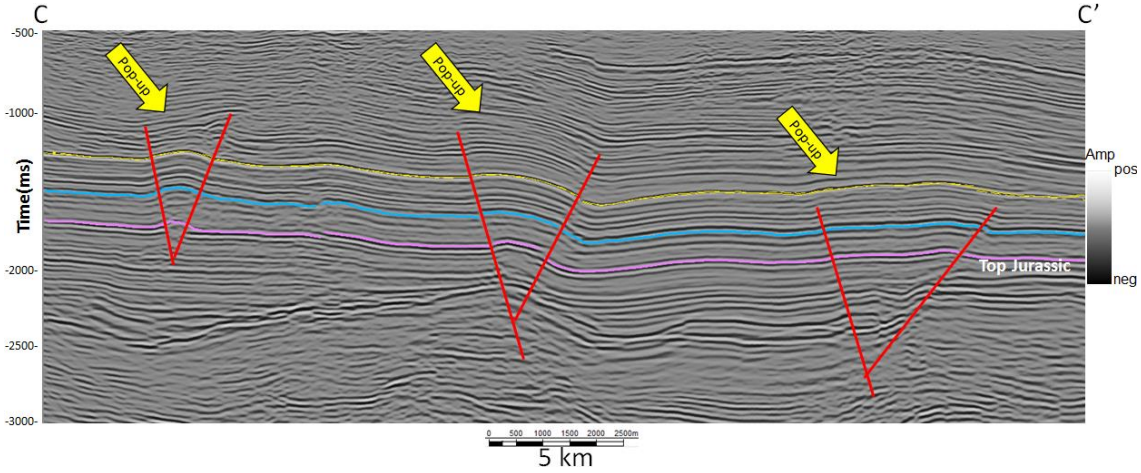

Figure 3.16. Interpreted seismic amplitude vertical slice C-C' shown in Figure 3.13. The figure is plotted with vertical exaggeration 3:1. The faults are illuminated in red color, whereas pop-up structures are indicated by yellow block arrows. Pink color picked horizon shows top Jurassic level horizon.

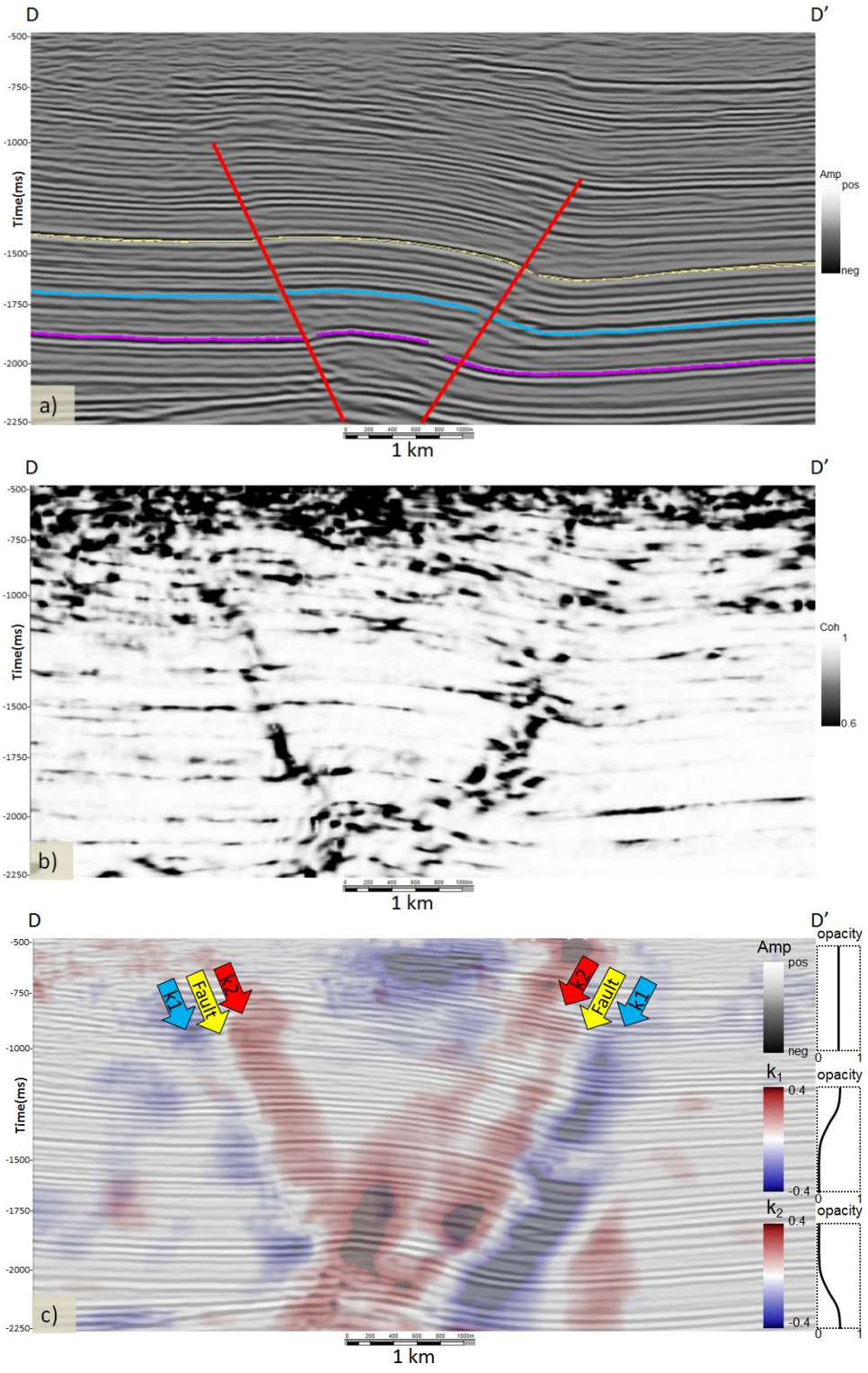

Figure 3.17. (a) Seismic amplitude, (b) Sobel filter similarity, (c) seismic amplitude blended with k_1 and k_2 vertical slices D-D'. Figure displayed with 1:1 ratio.

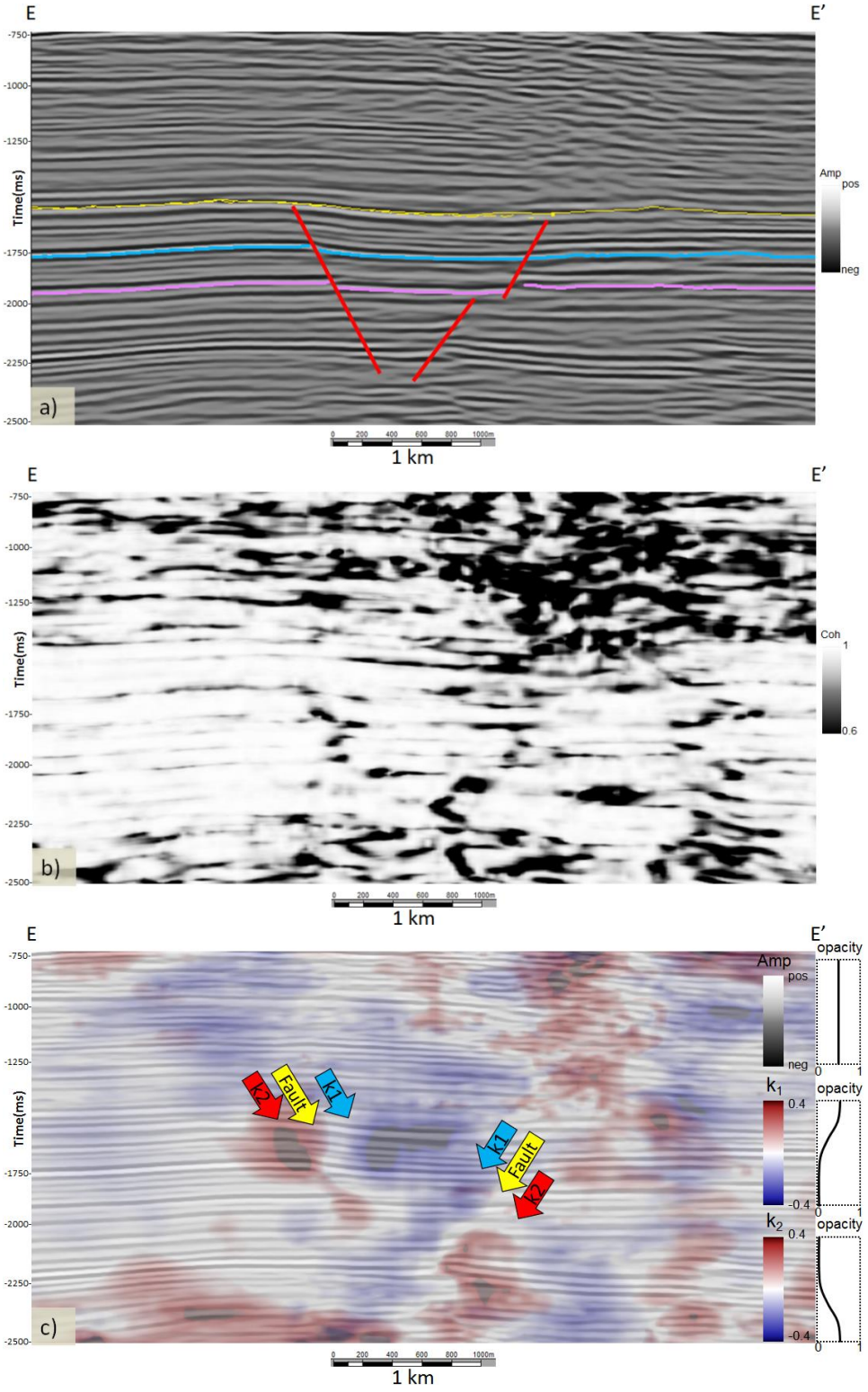

Figure 3.18. (a) Seismic amplitude, (b) Sobel filter similarity, (c) seismic amplitude blended with k_1 and k_2 vertical slices E-E'. Figure displayed with 1:1 ratio.

Chapter 4: Seismic Modeling of Tectonic Structures

In structurally-complex areas such as Chicontepec Basin, the details of tectonic structures directly impact production rates. The seismic expression of such structures is a function of the acquisition program, seismic wave propagation, and imaging as well as the underlying geology. In this chapter I generate two seismic models to define and illustrate the complex structures in the area. Specifically, I use a popular commercial finite difference wave-equation modeling software package to evaluate the pop-up and graben structures. I construct both models assuming that they have parallel bedding geometries with no significant thickness change along the beds. In both models, I use 121 sources with 50 m source spacing and 241 receivers with 25 m receiver spacing, values similar to those used in the Amatitlán survey. In both models, I use a Ricker wavelet with 25 Hz dominant frequency as the source wavelet, and generate raw common shot gathers. These common shot gathers are then prestack time and depth migrated using a Kirchhoff migration algorithm. Finally, seismic attributes are computed on both models, and the results compared to those computed from the real data. The values of the P-wave velocity and density are taken from a typical well log of the area (Figure 4.1).

Seismic modeling of a pop-up structure

The pop-up model shown in Figure 4.2 is constructed based on a vertical slice from the Amatitlán survey shown in Figure 3.17, in order to make the model geologically as consistent to those seen in the Chicontepec Basin, but not exactly the same. Simplification aids in extracting key information from the seismic modeling and imaging workflow. If the model is as complicated as the real geology, the modeling

results would be as difficult to interpret as the real data. In the model, there are two symmetric reverse faults on either side of the pop-up block. Both faults have a 25 m throw. The units above the top Paleocene level horizon are deformed, but not faulted. On the other hand, the units below the top Paleocene are deformed and faulted. I assume that formation velocities increase with depth. Figure 4.3 shows the prestack time and depth migrated seismic sections of the pop-up model. The depth migrated section provides a much better image than the time migrated section. While time migration works well for smooth velocities and flat reflectors, it cannot handle velocity changes in the overburden. In contrast, depth migration uses a detailed interval velocity model, and accurately handles velocity changes. Because of the abrupt velocity changes in the area, prestack depth migration works much better than prestack time migration on the pop-up model extracted from the Amatitlán survey. For this reason, I use prestack depth migrated synthetic data to compute seismic attributes. Figure 4.4 shows two snapshots generated from a source located in the middle of the model. Thin-bedded turbidites cause large amount of multiples. Figure 4.5a shows the depth migrated seismic amplitude section of the pop-up model in gray scale. Figure 4.5b shows the Sobel filter similarity attribute computed from the data shown in Figure 4.5a. The two symmetric reverse faults are successfully imaged, with low similarity anomalies seen on this vertical slice. However, unfaulted but deformed units cannot be identified on the similarity slice. Figure 4.5c shows a blended image of curvature and seismic amplitude. For both faults, positive curvature anomalies are observed (in red) on the upthrown blocks, whereas negative curvature anomalies are observed (in blue) on the downthrown blocks. Compared to the similarity attribute, curvature delineates not only the two

symmetric reverse faults, but also the unfaulted but deformed units. Figure 4.6 shows a blended image of the most-positive principal curvature, k_1, the most-negative principal curvature, k_2, and Sobel filter similarity for the real data from Amatitlán survey. Figure 4.7 shows the blended image of curvature and Sobel filter similarity for our pop-up model. Although the fault inclinations and placements are not exactly the same, the results computed from the model are quite similar to the results computed from the real data, thereby quantifying our interpretation of the attribute anomalies.

Seismic modeling of a graben structure

The graben model shown in Figure 4.8 is constructed from the vertical slice through the Amatitlán survey shown in Figure 3.18. As with the previous pop-up model I use the real data to construct a model that is geologically as consistent as possible, while maintaining simplicity to aid subsequent interpretation. In the graben model, the unit thicknesses, P-wave velocity and density values are kept same as those used in the pop-up model. There are two symmetric normal faults on either side of the graben structure. Both faults have a 25 m throw. The units above the top Paleocene level horizon are not deformed or faulted, while the units below the top Paleocene are faulted. I assume that velocity increases with depth. Figure 4.9 shows the prestack time and depth migrated seismic sections of the graben model. The depth migrated section provides a much better focused image than the time migrated section, delineating the fault edges. Figure 4.10a shows seismic amplitude section of the prestack depth migrated data in gray scale. Figure 4.10b shows the Sobel filter similarity attribute computed from the data shown in Figure 4.10a. The two symmetric normal faults appear as low similarity anomalies on this vertical slice. Figure 4.10c shows blended

image of curvature and seismic amplitude. For both faults, positive curvature anomalies are observed (in red) on the upthrown blocks, whereas negative curvature anomalies are observed (in blue) on the downthrown blocks. Similar to the Sobel filter similarity attribute, curvature attribute leads us to identify the two symmetric normal faults successfully. Figure 4.11 shows blended image of the most-positive principal curvature, k_1, the most-negative principal curvature, k_2, and Sobel filter similarity for the real data from Amatitlán survey. Figure 4.12 shows blended image of curvature and Sobel filter similarity for our graben model. Although the fault inclinations and placements are not exactly the same, the results computed from the model are similar to the results computed from the real data. This calibrates our interpretation of attributes over the graben seen in Figure 3.18.

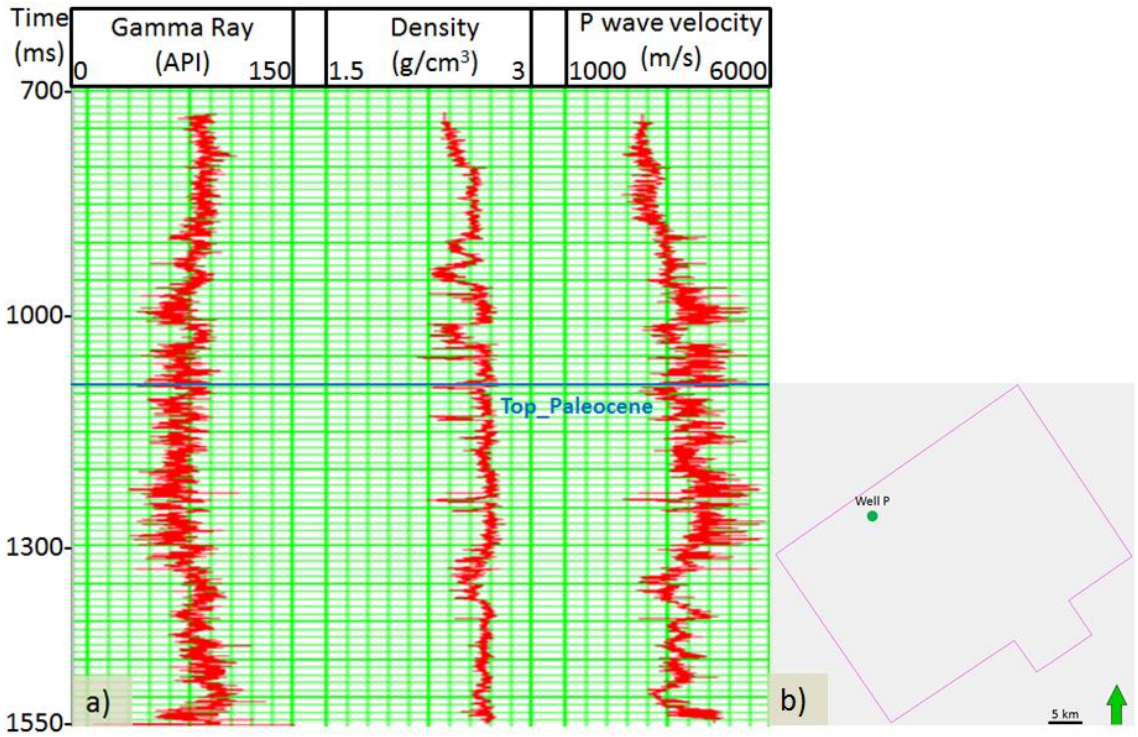

Figure 4.1. (a) A representative well, P, in the study area showing gamma ray, density, and P-wave sonic logs, (b) location of the well.

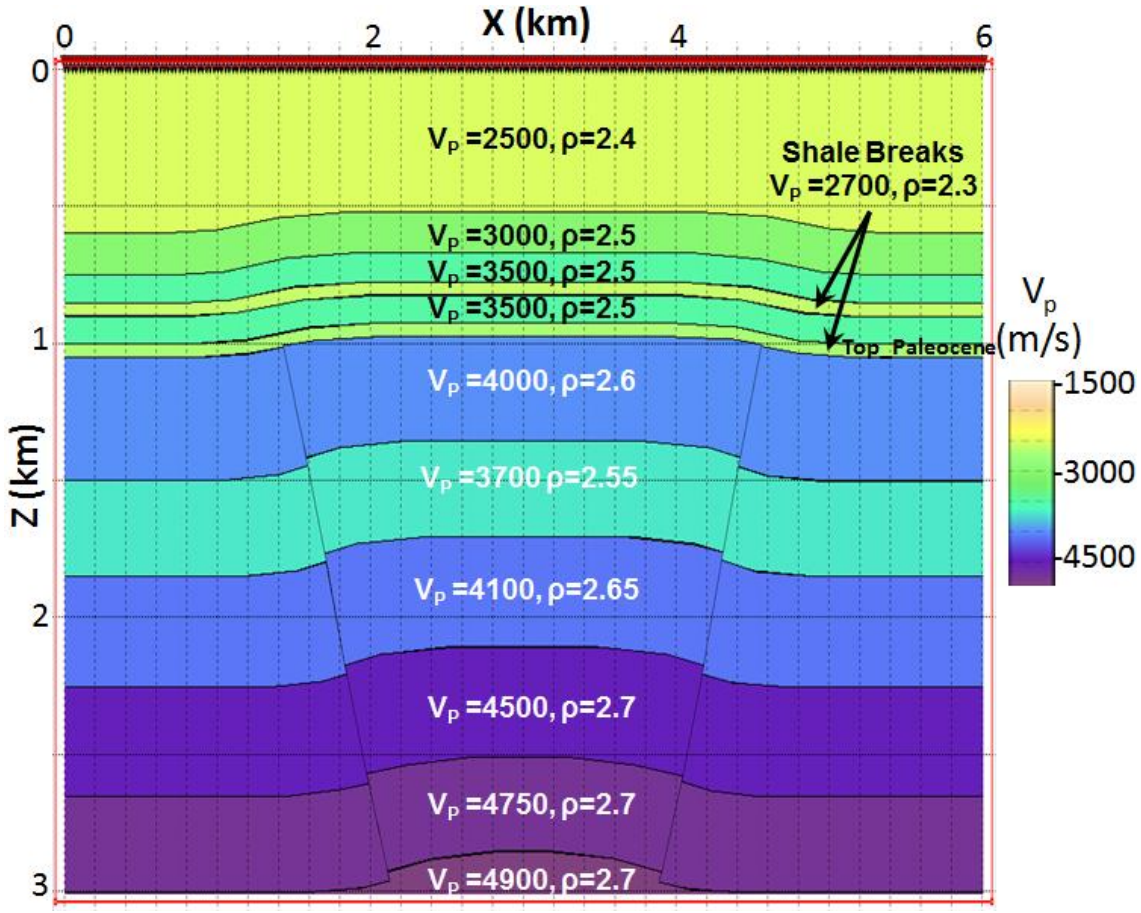

Figure 4.2. Symmetric pop-up model extracted from Amatitlán survey. The units below the top Paleocene are faulted. P-wave velocity V_P is in m/s while density ρ is in g/cm^3.

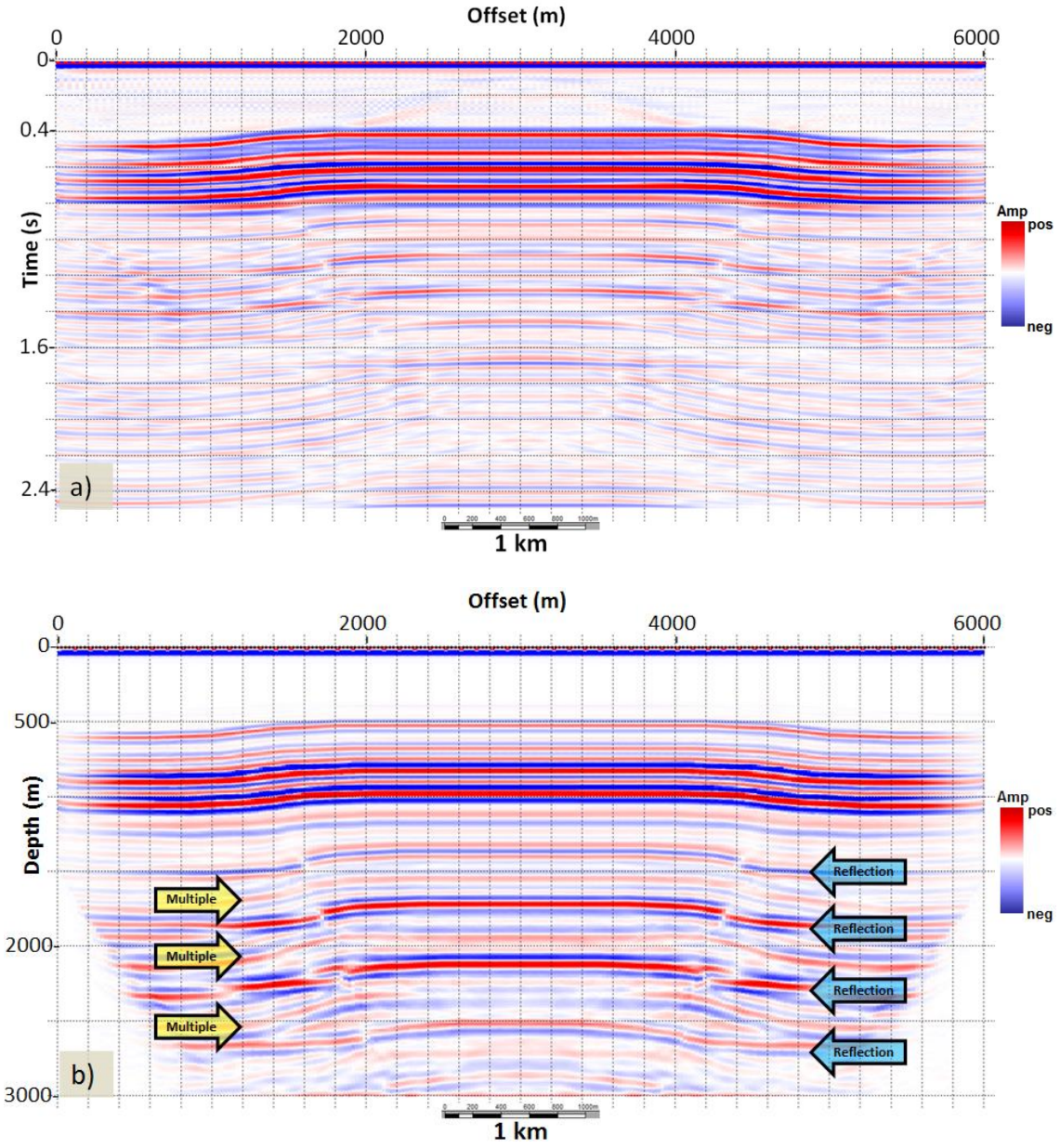

Figure 4.3. (a) Prestack time migrated seismic section, (b) prestack depth migrated seismic section of the pop-up model shown in Figure 4.2. Note that the depth migration provides a sharper image of the fault discontinuities. Yellow arrows indicate multiples, while blue arrows indicate reflections.

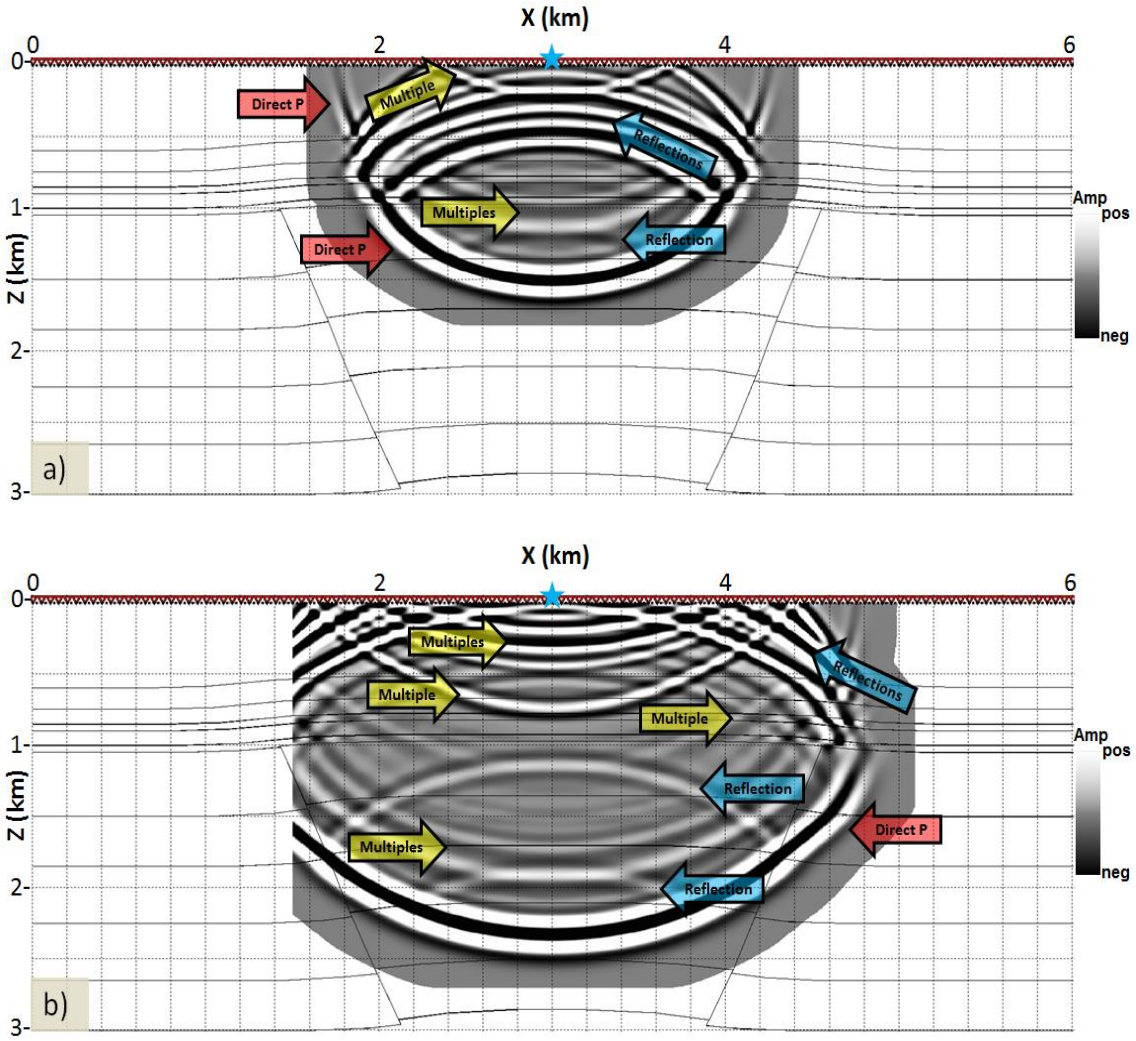

Figure 4.4. Snapshots at (a) t=0.5 s, (b) t=0.7 s for a shot location indicated by the blue star. Yellow arrows indicate multiples, blue arrows indicate reflections, and red arrows indicate direct waves. Thin-bedded model generates a large amount of multiples. Note the lack of energy from the deeper reflections.

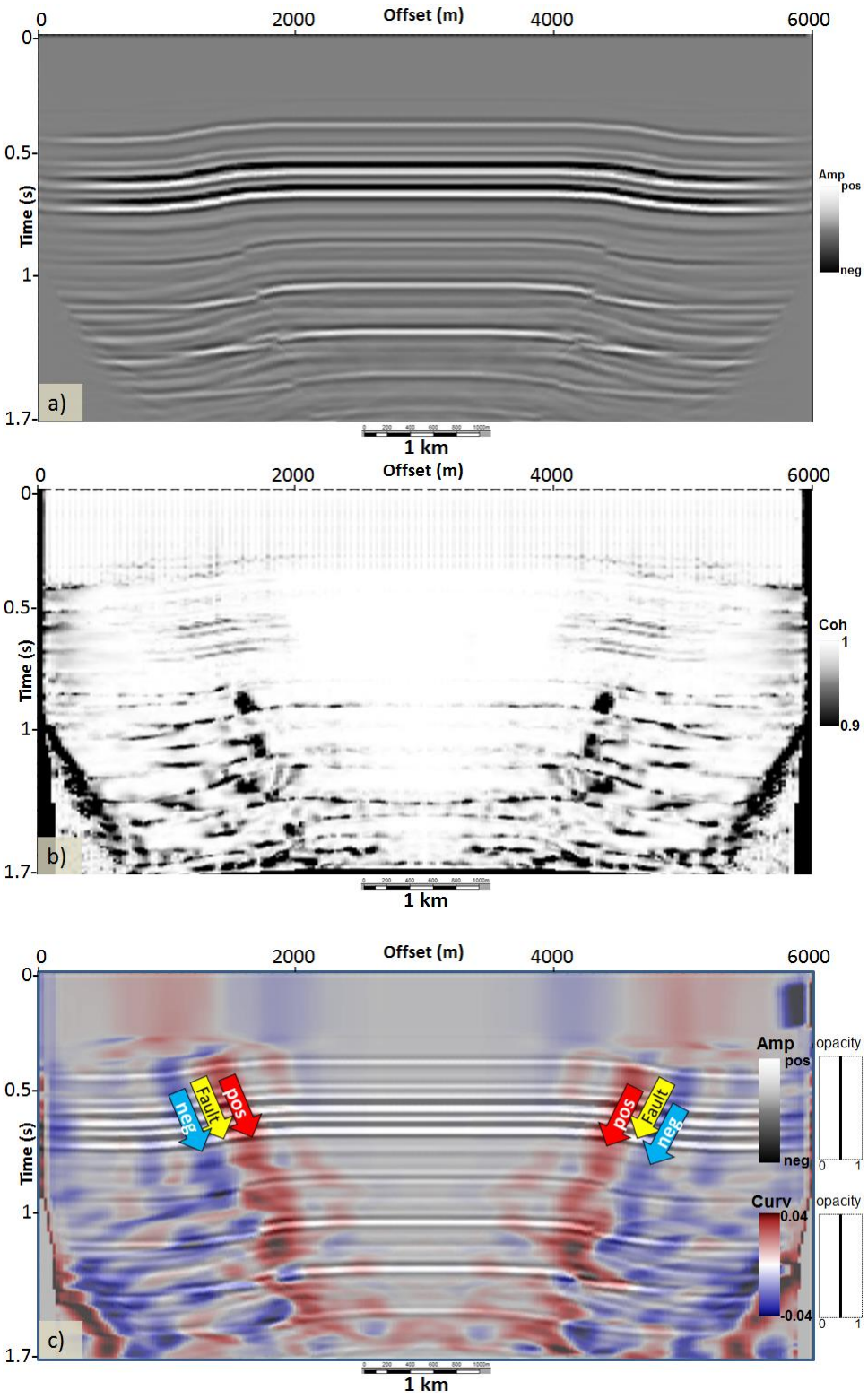

Figure 4.5. (a) Prestack depth migrated seismic amplitude, (b) Sobel filter similarity, (c) seismic amplitude blended with curvature for the pop-up model shown in Figure 4.2.

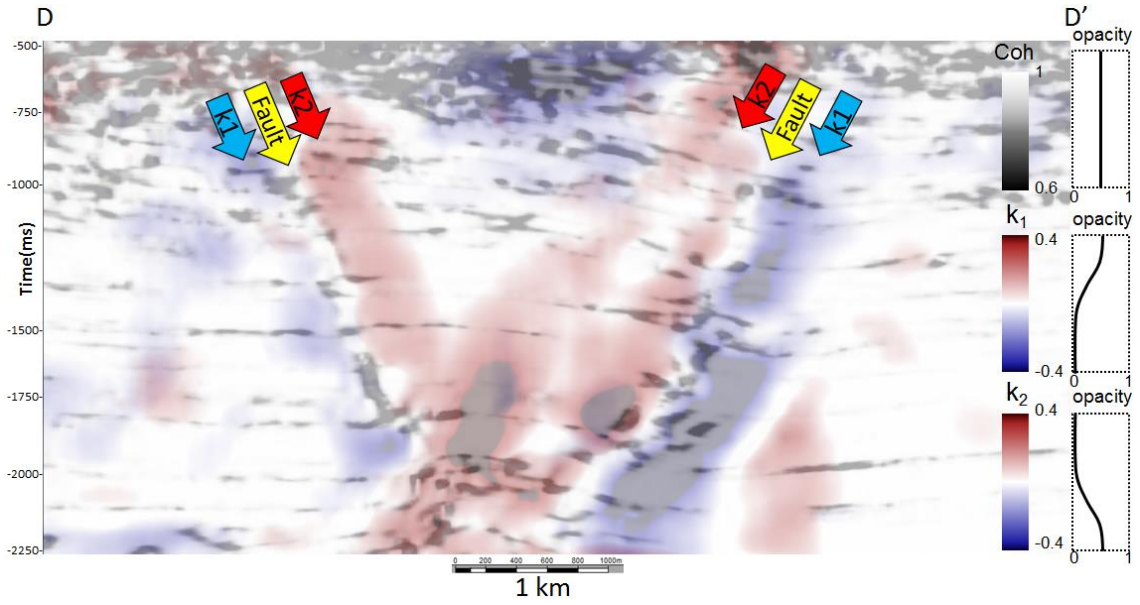

Figure 4.6. Sobel filter similarity blended with *k1* and *k2* vertical slices along line D-D' through the Amatitlán survey shown in Figure 3.14.

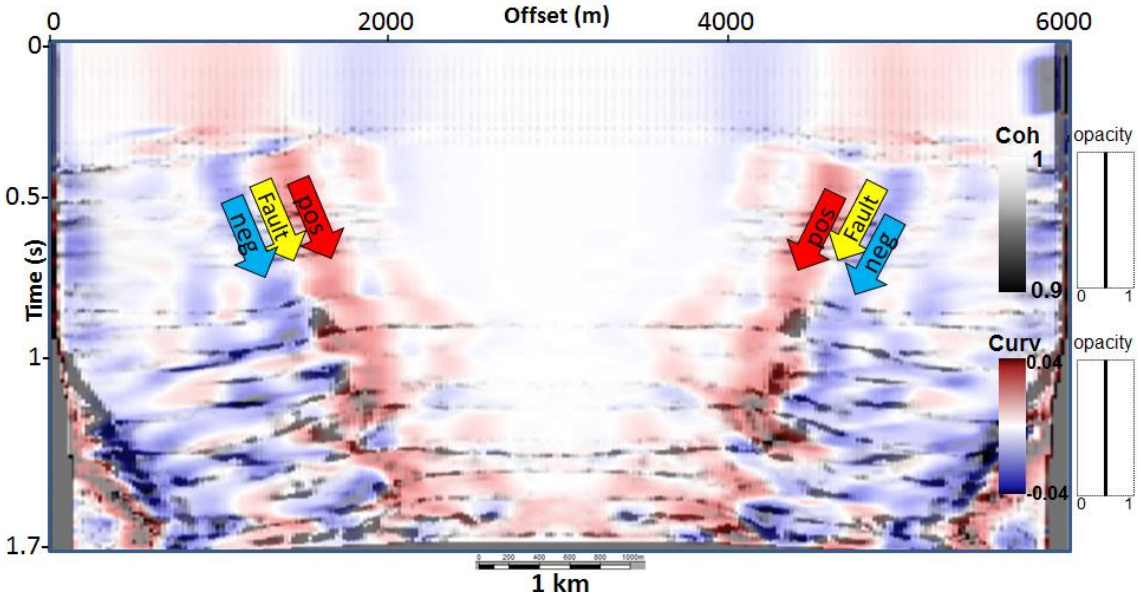

Figure 4.7. Sobel filter similarity blended with curvature for the pop-up model. Note that the results computed from the model are similar to the results computed from the real data.

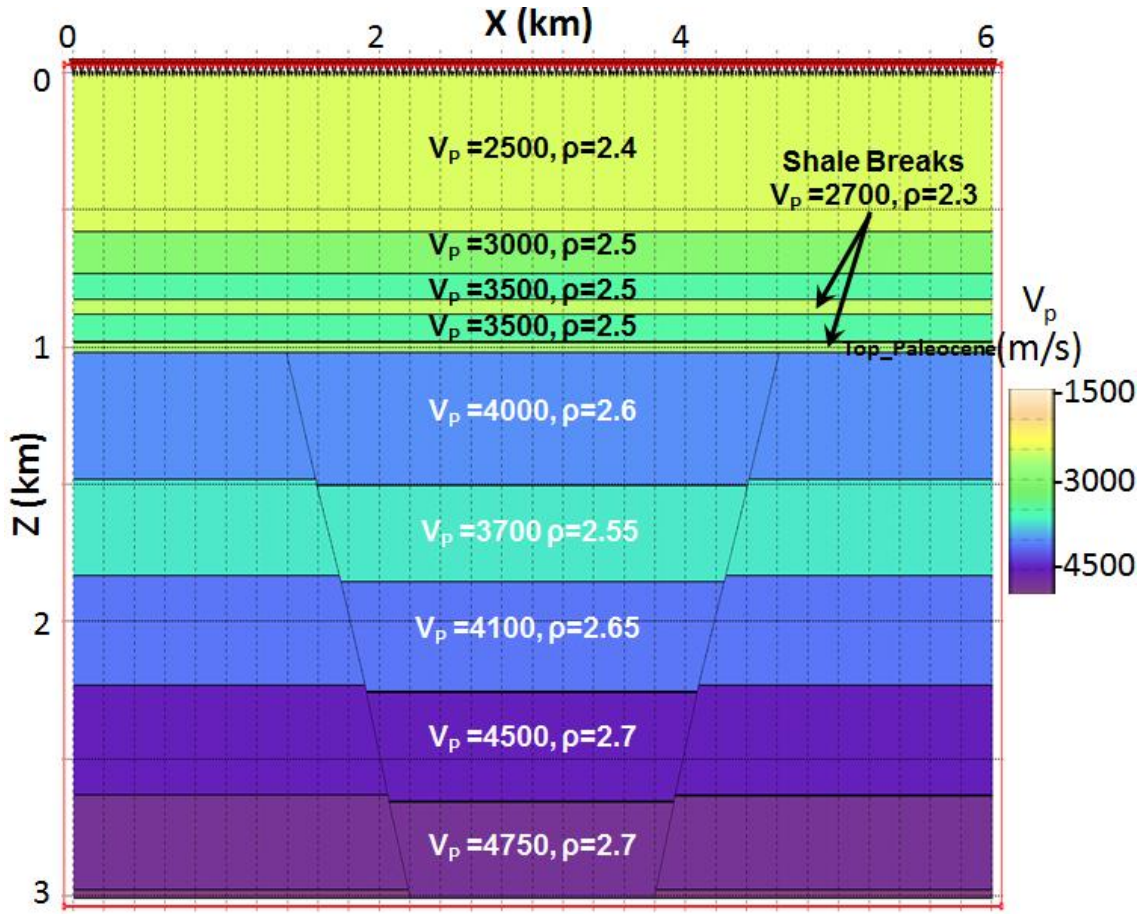

Figure 4.8. Graben model extracted from the Amatitlán survey. The units below the top Paleocene are faulted. P-wave velocity V_P is in m/s while density ρ is in g/cm^3.

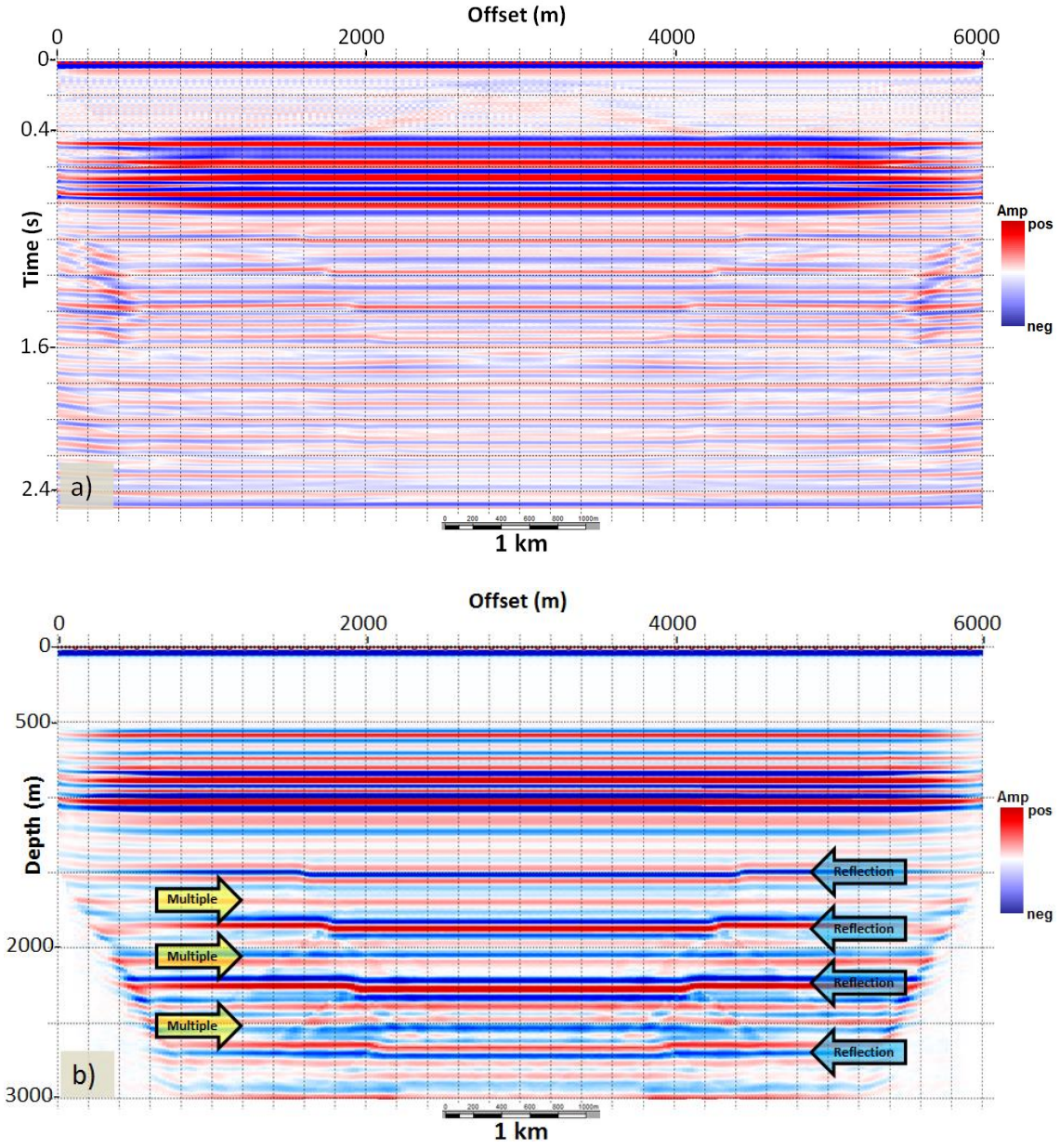

Figure 4.9. (a) Seismic amplitude from prestack time migration and (b) prestack depth migration of the synthetic data from graben model shown in Figure 4.8. Note that the faults in the depth migrated image are much better resolved. Yellow arrows indicate multiples, while blue arrows indicate reflections.

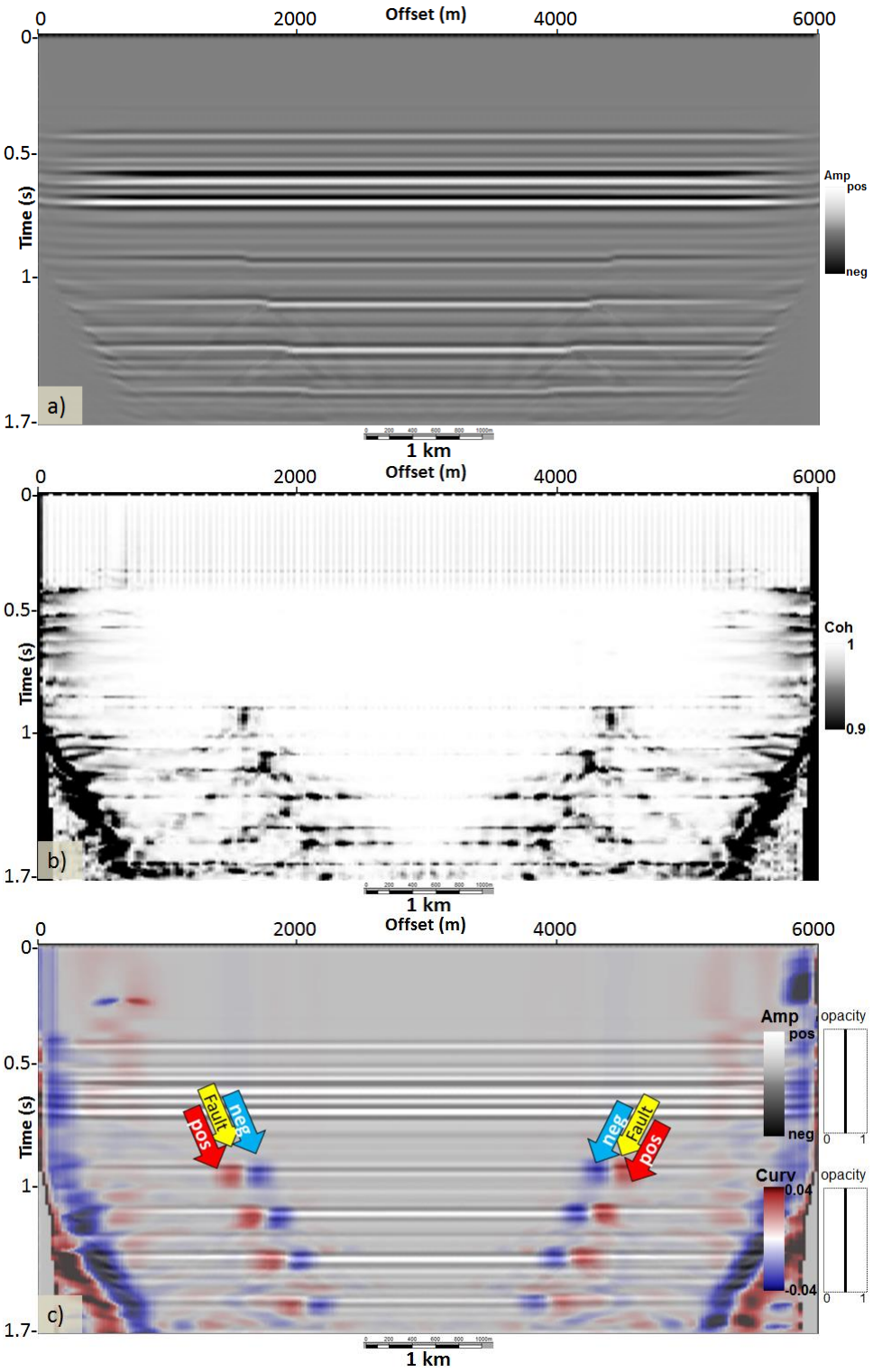

Figure 4.10. (a) Prestack depth migrated seismic amplitude, (b) Sobel filter similarity, (c) seismic amplitude blended with curvature for the graben model shown in Figure 4.8.

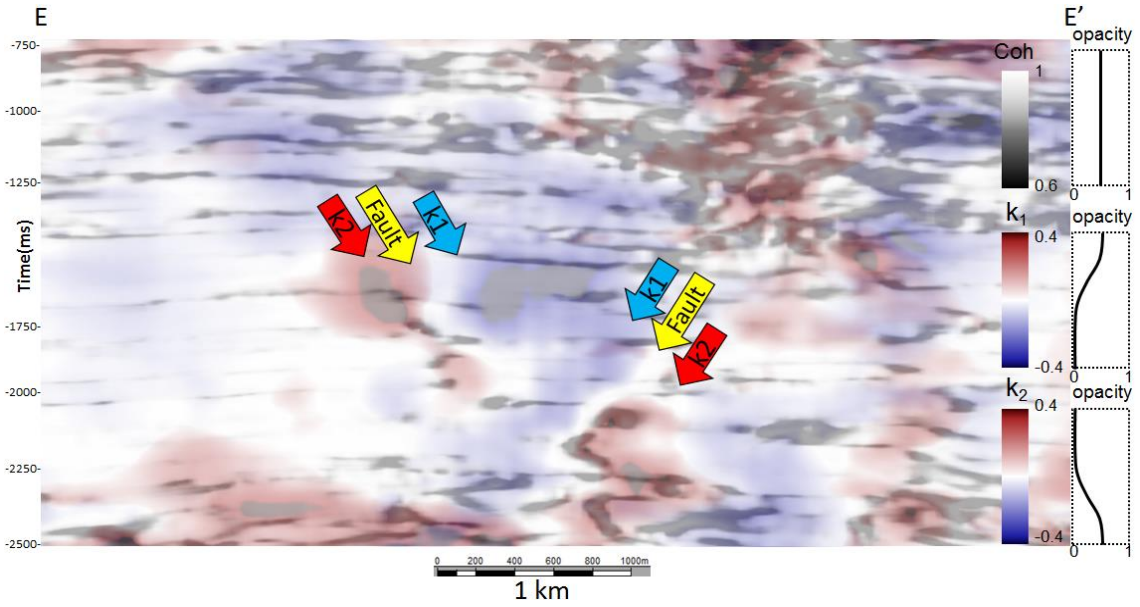

Figure 4.11. Sobel filter similarity blended with *k1* and *k2* vertical slices along line E-E' shown in Figure 3.14.

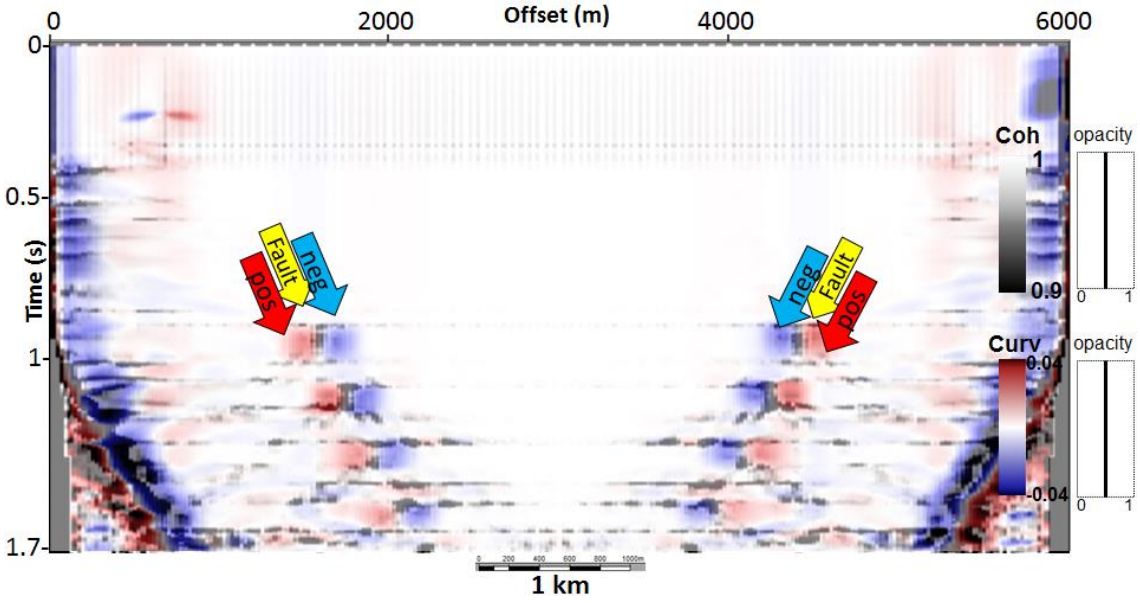

Figure 4.12. Sobel filter similarity blended with curvature for the graben model. Note that the results computed from the model are similar to the results computed from the real data.

Chapter 5: Prestack Data Conditioning

The data were originally acquired and processed in 2003 by PEMEX Exploration and Production. However, to obtain better shallow imaging and to attenuate low frequency noise, the Amatitlán survey was reprocessed by PEMEX Exploration and Production in 2007. Although the 2007 reprocessed data is better than the 2003 data, I try to further improve the prestack data quality and increase the frequency content by applying residual velocity analysis, non-stretch NMO correction, and prestack structure oriented filtering to the prestack seismic gathers.

Velocity analysis

One of the more important steps in processing is velocity analysis, which consists of calculating NMO or migration velocities by aligning traces measured at different offsets, flattening the hyperbolic events in the prestack gathers. Angle-dependent inversion and AVO assume that the reflectors within a gather have been properly corrected to be flat. In time migration, if the velocity is too low, the reflection is overcorrected, and curves upwards. If the velocity is too high, the reflection is undercorrected, and curves downwards.

The original data were prestack time migrated using a Kirchhoff algorithm into 50 m offset bins ranging between 50 and 3000 m. The original migration velocities were then removed using a simple reverse NMO correction. I then perform a dense residual velocity analysis on a 250 m x 250 m grid (every 10^{th} inline and crossline) to flatten the gathers, scanning velocities ranging from 1000 m/s to 7000 m/s. The workflow used for residual velocity analysis is shown in Figure 5.1. The inputs for velocity analysis are seismic amplitude and semblance, and the output is a velocity file.

Figure 5.2 shows a part of the base map of the Amatitlán survey, on which I pick the reflector velocities. Green points indicate picked CMPs; red points indicate unpicked CMPs, while the yellow point indicates the current CMP shown in Figure 5.5a. Figure 5.3 shows the semblance analysis where white squares show picked velocities.

MPNMO correction

The next step after velocity analysis is a new NMO correction to flatten the prestack seismic gathers. MPNMO (non-stretch NMO), introduced by Zhang et al. (2013), is a matching-pursuit-based normal moveout correction used to minimize NMO stretch effects in long-offset data, thereby increasing the frequency content of the data. To avoid stretching the nonzero offset traces, the moveout correction needs to be constant for all samples. MPNMO processes the data wavelet-by-wavelet rather than sample-by-sample, and avoids wavelet stretch effects at far offsets. Figure 5.4 shows the flowchart for MPNMO correction. The inputs for MPNMO include the undercorrected seismic data (the migrated gather after reverse NMO) and the velocity file obtained from velocity analysis**.** The output is non-stretch NMO corrected prestack gathers. The standard NMO correction causes wavelet stretching at far offsets that lowers the frequency content of the seismic data. The part with severe stretching is usually muted from the data, resulting in reduced leverage against multiples and reduced accuracy shear impedance estimates. By reducing stretch, MPNMO obviates the need to mute the long-offset data. Frequency content is preserved, resolution is increased, and more far offset data are provided for prestack inversion (Zhang et al., 2013).

Figure 5.5 shows a prestack gather before and after MPNMO correction. Figure 5.6a shows the frequency spectrum of original prestack time migrated data. Figure 5.6b shows the frequency spectrum after performing detailed velocity analysis and MPNMO correction. Significant frequency enhancement and improved resolution are observed after residual velocity analysis and MPNMO correction compared to the original data.

Prestack structure oriented filtering

After MPNMO correction, I apply a prestack structure oriented filter (SOF) to the prestack time migrated common offset gathers using a workflow described by Kwiatkowski and Marfurt (2011) (Figure 5.7). In prestack SOF, reflector dip and similarity computed from the stacked volumes are used to guide the prestack data filter. For these data I use an edge-preserving mean filter along reflector dip to remove random noise, thereby preserving lateral discontinuities. Figure 5.8a and Figure 5.8b shows common reflection point gathers before and after applying prestack structure oriented filtering to common offset volumes. Figure 5.8c shows the rejected signal plotted at the same scale. Most of the incoherent noise is removed and cleaner data are observed after structure oriented filtering. The result is signal-enhanced prestack gathers suitable for prestack angle-dependent inversion.

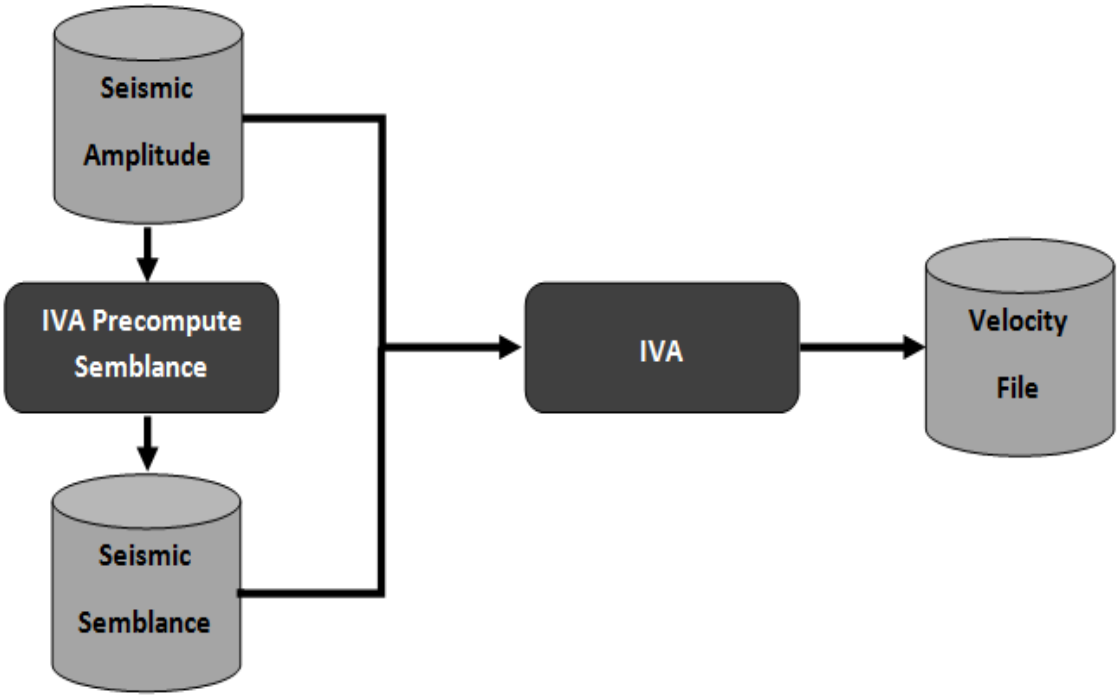

Figure 5.1. Velocity analysis workflow. For the IVA (interactive velocity analysis), the inputs are seismic amplitude and semblance, and the output is a velocity text file.

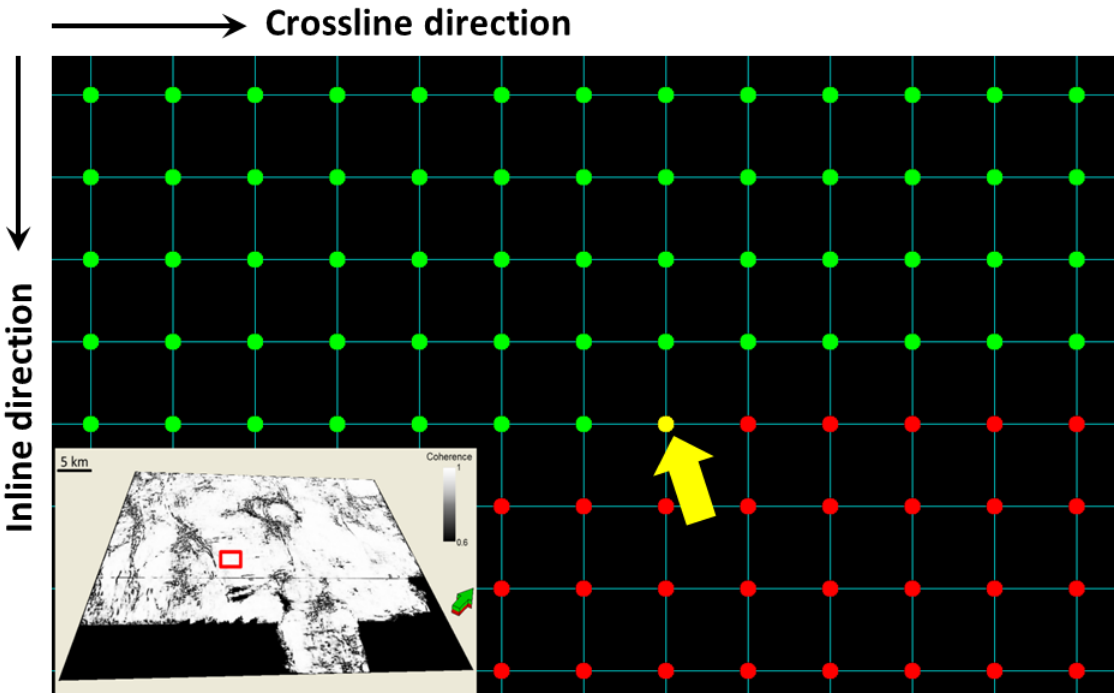

Figure 5.2. Base map of the Amatitlán survey. Location indicated by red rectangle. Green points indicate previously picked CMPs, red points indicate unpicked CMPs, while the yellow point shown by the block arrow indicates the current CMP shown in Figure 5.5a.

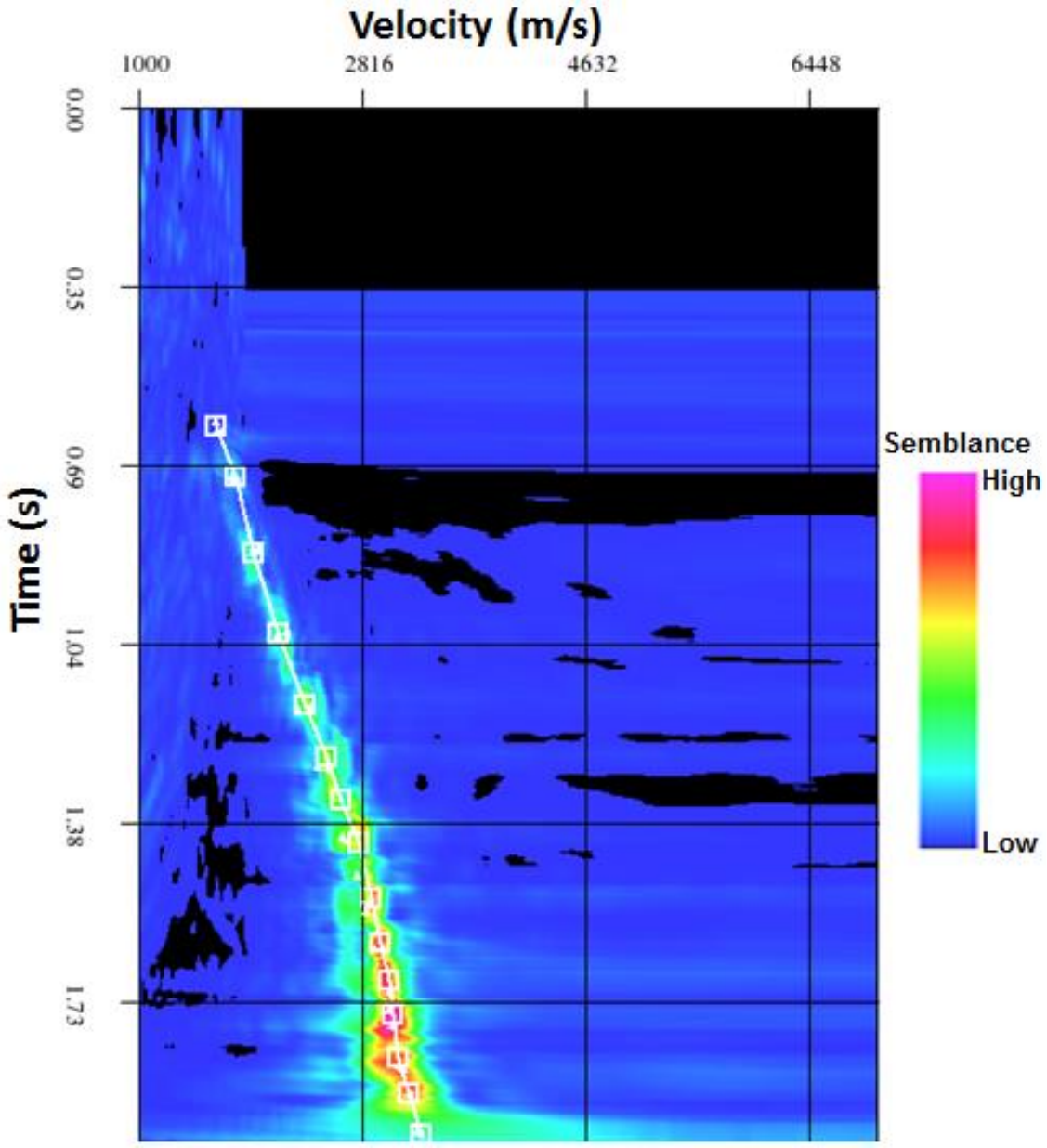

Figure 5.3. Velocity analysis for the CMP gather shown in Figure 5.5a. White squares indicate picked velocities.

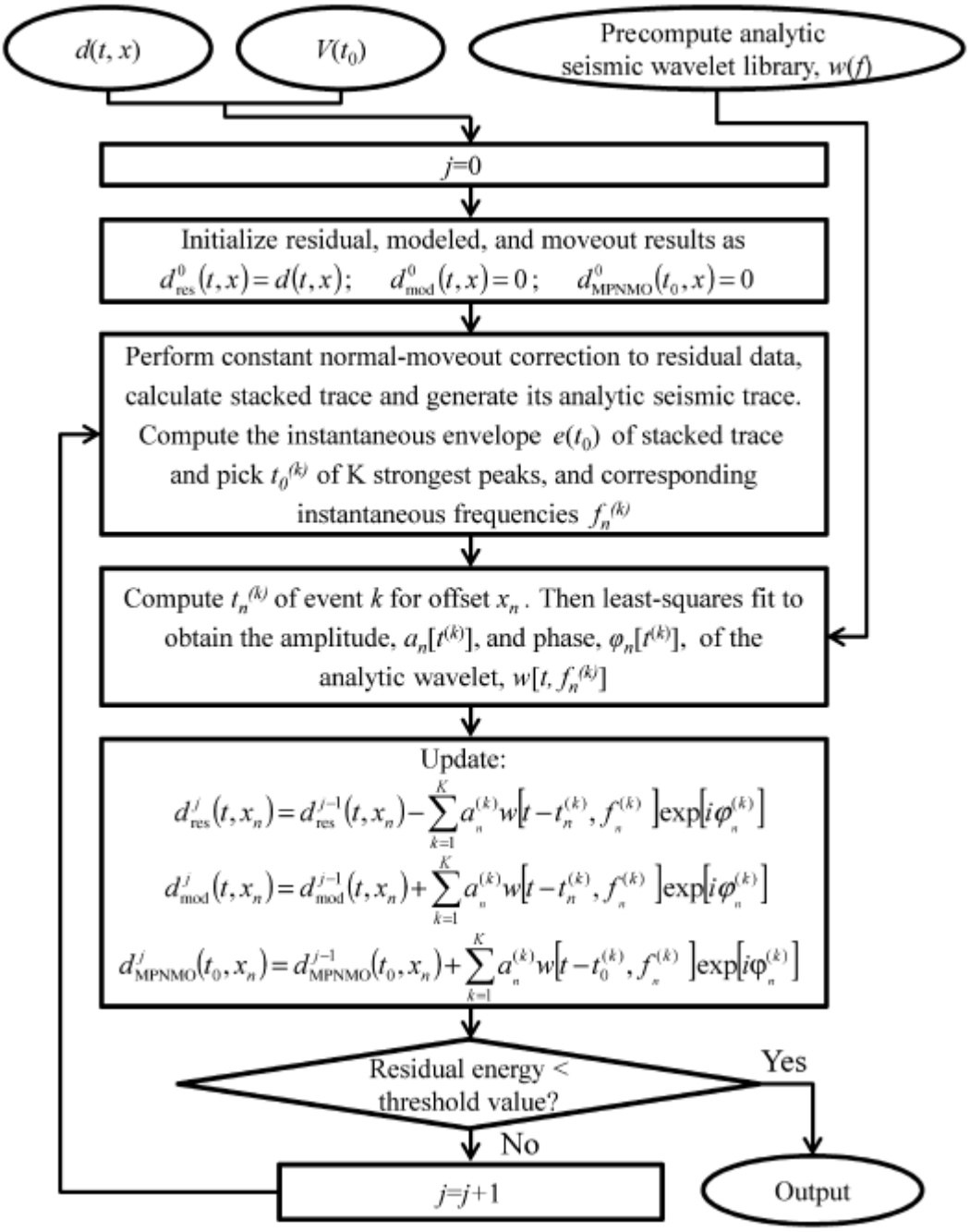

Figure 5.4. MPNMO (Non-stretch NMO) correction workflow. Instead of sample-by-sample, the correction is implemented on a wavelet-by-wavelet basis (After Zhang et al., 2013).

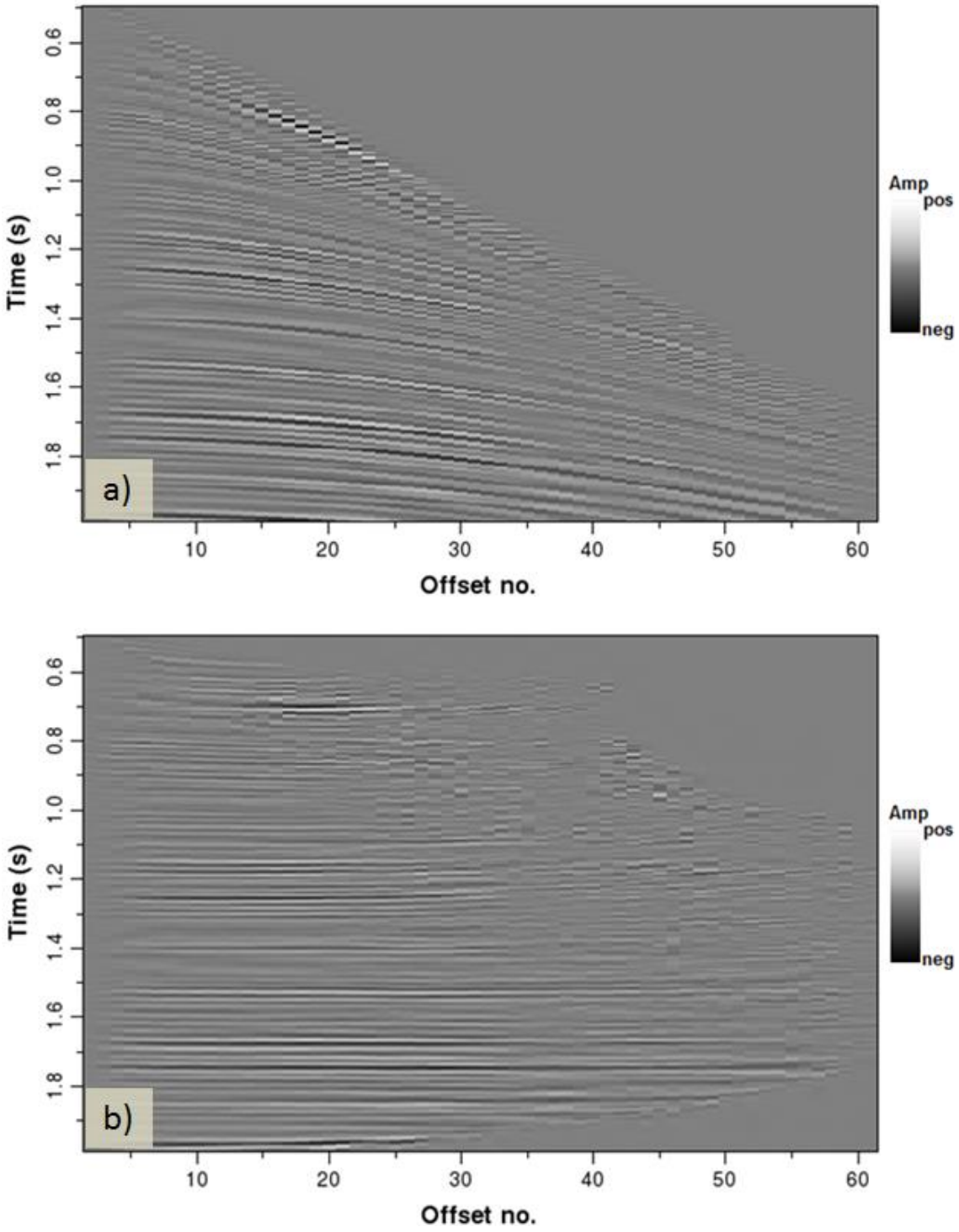

Figure 5.5. Prestack seismic gathers (a) before, and (b) after MPNMO correction for the yellow CMP location, using the velocity picks shown in Figure 5.3.

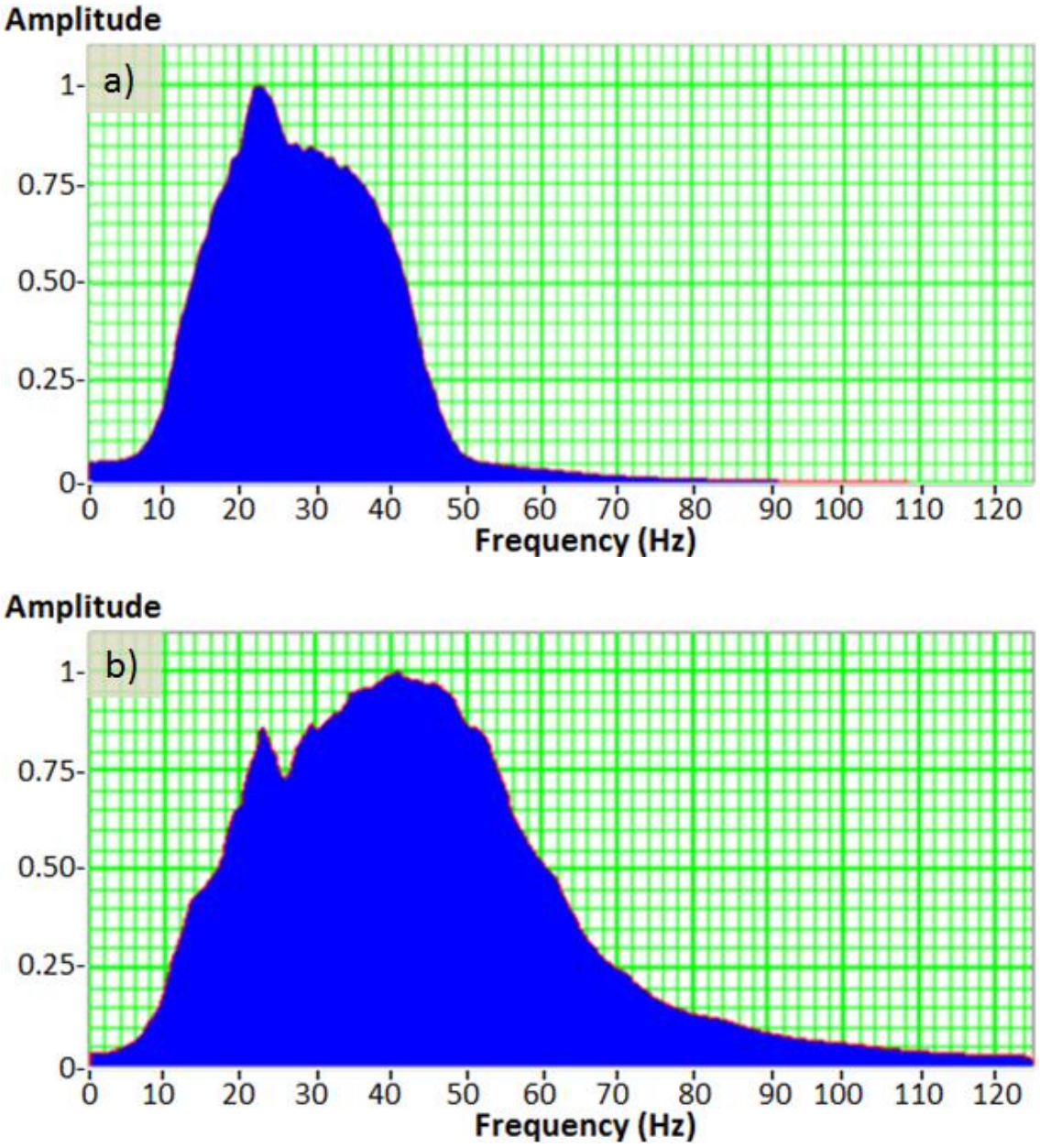

Figure 5.6. (a) Frequency spectrum of the original prestack time migrated data, (b) frequency spectrum after performing detailed velocity analysis and MPNMO correction. Significant increase in frequency content is observed after residual velocity analysis and MPNMO correction compared to the original data.

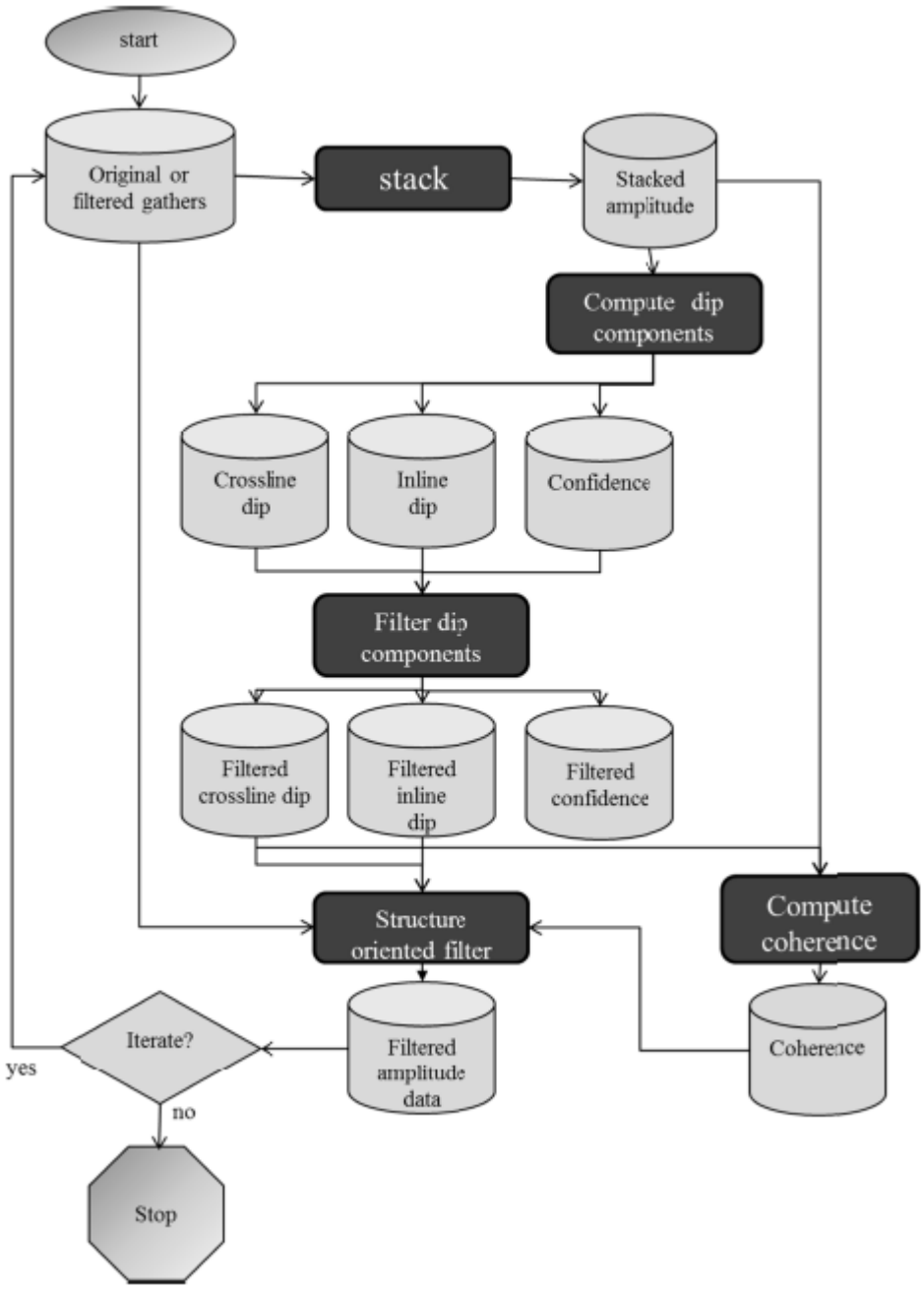

Figure 5.7. Prestack structure oriented filtering workflow (After Kwiatkowski and Marfurt, 2011).

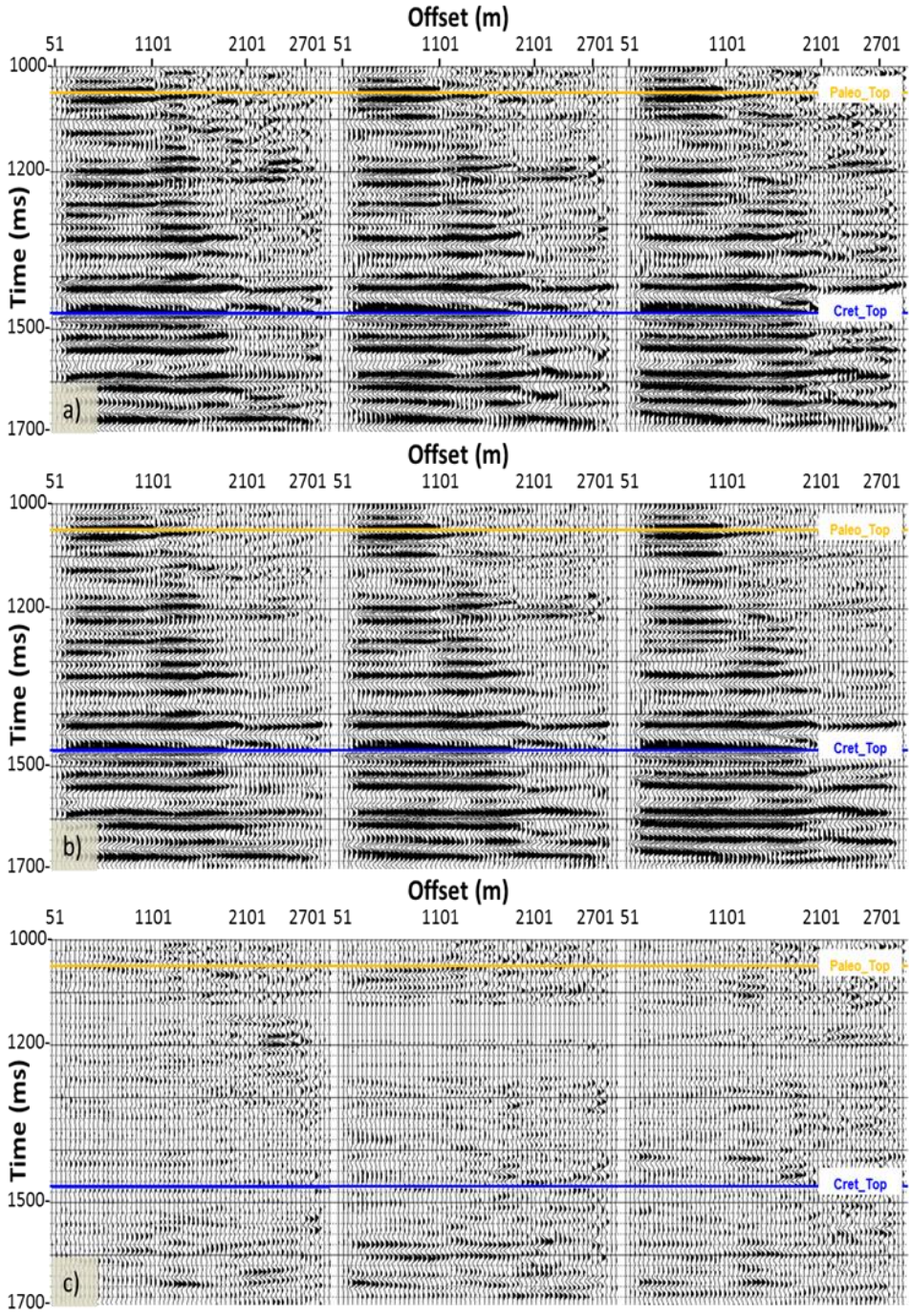

Figure 5.8. Migrated common reflection point gathers (a) before and (b) after prestack structure oriented filtering, (c) the rejected signal plotted at the same scale. Orange horizon represents top Paleocene level and blue horizon represents top Cretaceous level. Note the cleaner data and improved signal-to-noise ratio after prestack structure oriented filtering.

Chapter 6: Simultaneous Prestack Seismic Inversion

Unlike seismic amplitude that measures relative changes in rock properties, seismic inversion is directly correlated to the rock properties of each formation (Swisi, 2009). Impedance is defined as the product of intrinsic properties of the rock such as P-wave velocity and density, ρV_P, and S-wave velocity and density, ρV_S. These rock properties can be obtained from well-log measurements. By tying the wells to the seismic amplitude, the seismic impedances provide estimates of rock properties that are used to characterize the reservoir.

To estimate the rock properties from seismic data, I perform prestack simultaneous angle-dependent inversion (Hampson et al, 2005) on the conditioned prestack CRP gathers. The following steps are involved in the inversion process:

- Tying the wells to seismic amplitude,
- Generating angle gather,
- Extracting angle-dependent wavelets,
- Low frequency modeling of Z_p and Z_s from the well logs and seismic horizons,
- Inverting the seismic data, and
- Plotting the error.

Well seismic tie

28 wells are tied to the seismic data having original sonic and density logs and unique extracted wavelets. The correlation coefficient for all tied wells varies between 0.62 and 0.87. Figure 6.1 shows a typical well log of the area (well P) tied to seismic data with a correlation coefficient of 0.791. The extracted wavelet from well P and correlation coefficient between logs and seismic for well P is shown in Figure 6.2.

Ideally, each of the tied wells has gamma ray, compressional wave as well as shear wave logs. However, only five of the wells in the area have dipole sonic and gamma ray information. Therefore, I derive a multilinear relationship between gamma ray, V_p and V_s from five wells in order to predict shear wave sonic logs where they do not exist (Figure 6.3).

Generating Angle gather

I use velocities from a typical well log of the Chicontepec area in order to convert the gathers from offset to angle domain. Only one velocity function is used to avoid introducing interpretation errors.

Extracting angle-dependent wavelets

Angle-dependent statistical wavelets are extracted near well P for three angle-limited gathers (near angle stack: 0-11°, mid angle stack: 12-22°, far angle stack: 23-33°). Figure 6.4 shows the wavelet time variations and frequency spectra for the extracted angle-dependent wavelets used for prestack inversion.

Low frequency modeling

The low frequency models for Z_p and Z_s are obtained from the well logs and picked seismic horizons through an interpolation process. Figure 6.5 shows the low frequency models for Z_p and Z_s corresponding to line F-F'.

Inversion results

I apply commercial model-based simultaneous inversion software to the preconditioned seismic gathers to obtain P-impedance (Z_p), S-impedance (Z_s), and density (ρ) volumes. Traces from the inversion volumes are compared at random well locations to quality control the inversion process. This quality check indicates a good

match between the original logs and inverted traces for Z_p, Z_s and density (Figure 6.6). Figure 6.7a shows original vertical seismic amplitude section corresponding to line F-F'. Figure 6.7b shows the same section after performing residual velocity analysis, MPNMO correction, and prestack SOF. Better definition of the units, higher resolution, frequency enhancement, and improved signal-to-noise ratio are observed after prestack data conditioning. The frequency spectra corresponding to each volume are shown in Figure 5.6. Inverted vertical slices along line F-F' through the Z_p and Z_s volumes are shown in Figure 6.8. The resolution is improved on the inverted slices compared to the seismic amplitude, providing a better resolution of the thin-bedded turbidites in the area. On the inverted volumes, relatively high impedance corresponds to sandstones whereas lower impedance corresponds to thin shale layers that separate the sandstone reservoirs in the Chicontepec Basin.

Error plot

Plotting the error is a crucial step in the inversion process, since it indicates how confident we are from the inversion results. To calculate the normalized RMS error, I first calculate the difference between real traces obtained from the seismic data and synthetic traces generated by the inversion process. Next, I take the absolute value to make the values all positive, and divide them by the trace RMS amplitudes of the angle gather to create relative error, making it independent of the amplitude variation from CMP to CMP. Finally, I stack the error traces, and normalize the error traces by dividing them by the number of angles to obtain the normalized relative RMS error volume. Very low amounts of error are observed throughout the entire error volume. Figure 6.9 and Figure 6.10 show error time slices at t=1200 ms and t=1400 ms. Both

figures are plotted against the same color scale. Both figures exhibit low error which proves the accuracy of the inversion process. In both time slices, less error are observed near the wells compared to their surrounding environments. Relatively high amount of error are observed on the deeper time slice. The wells that have been used in inversion only penetrate into the shallower Eocene-Paleocene section. Lack of well control in the deeper section causes this higher amount of error.

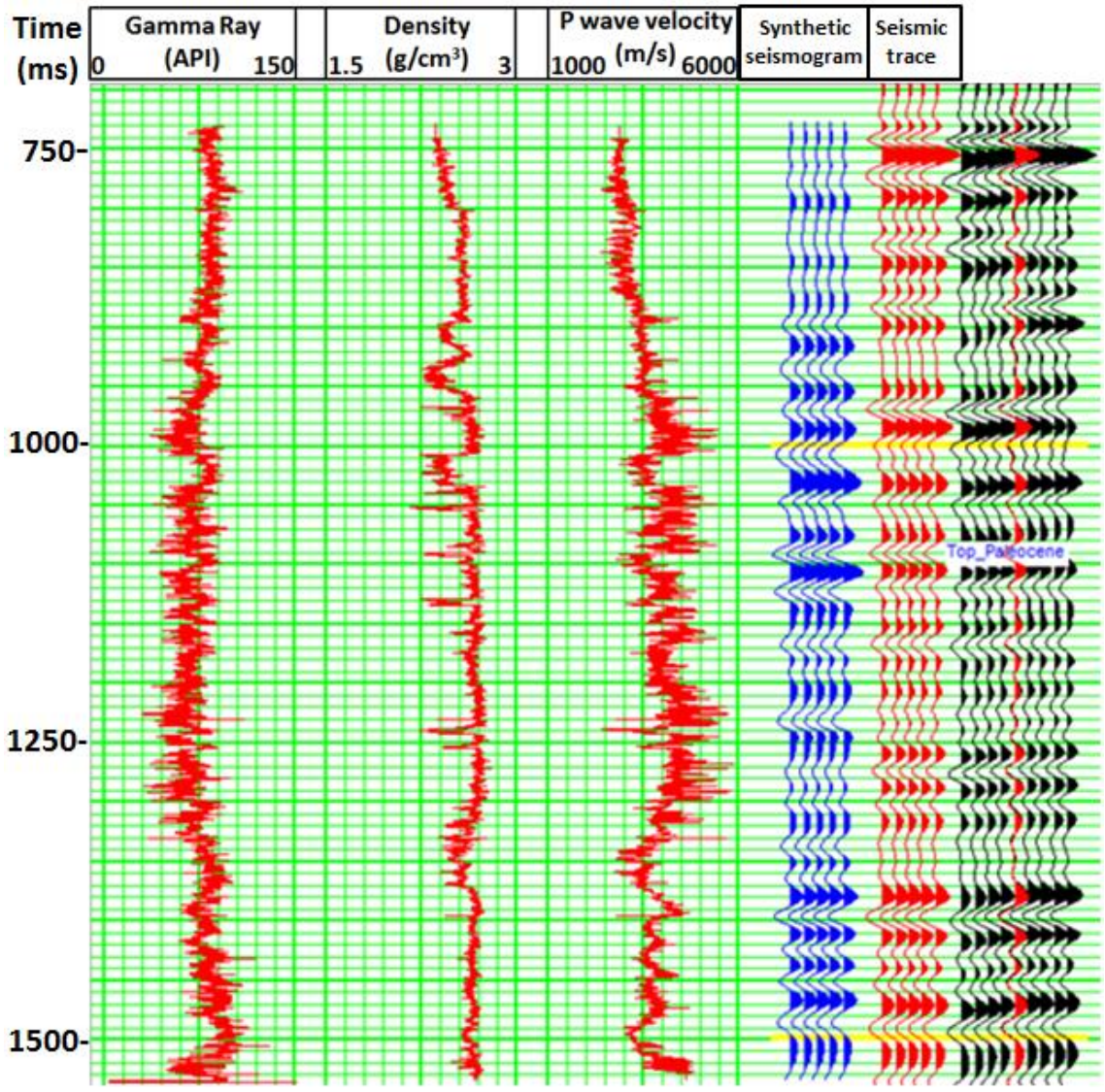

Figure 6.1. A typical well log of the area (well P) tied to seismic. Location of the well is shown in Figure 6.9.

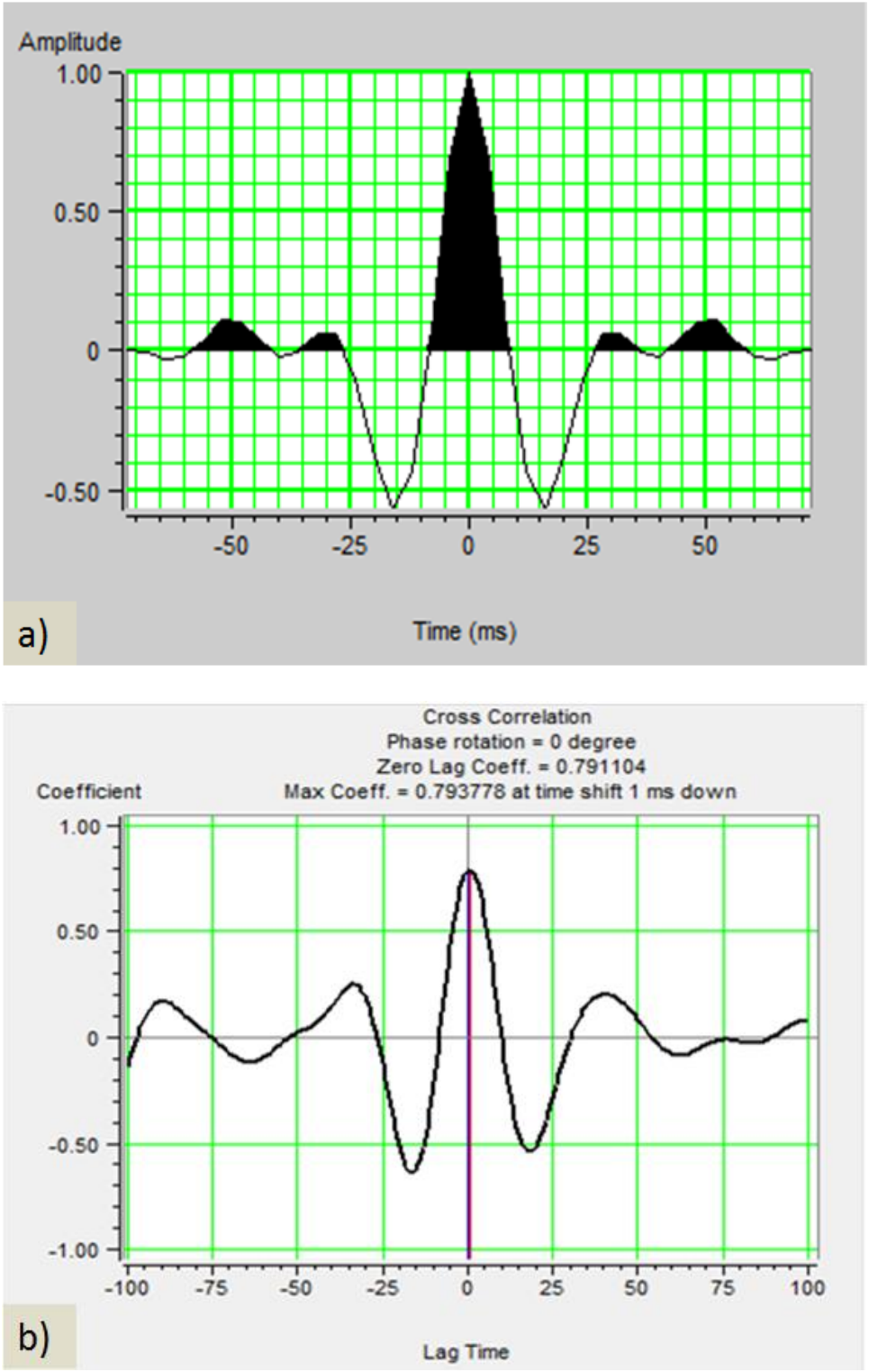

Figure 6.2. (a) Wavelet extracted from well P, (b) cross correlation coefficient for well P (0.791).

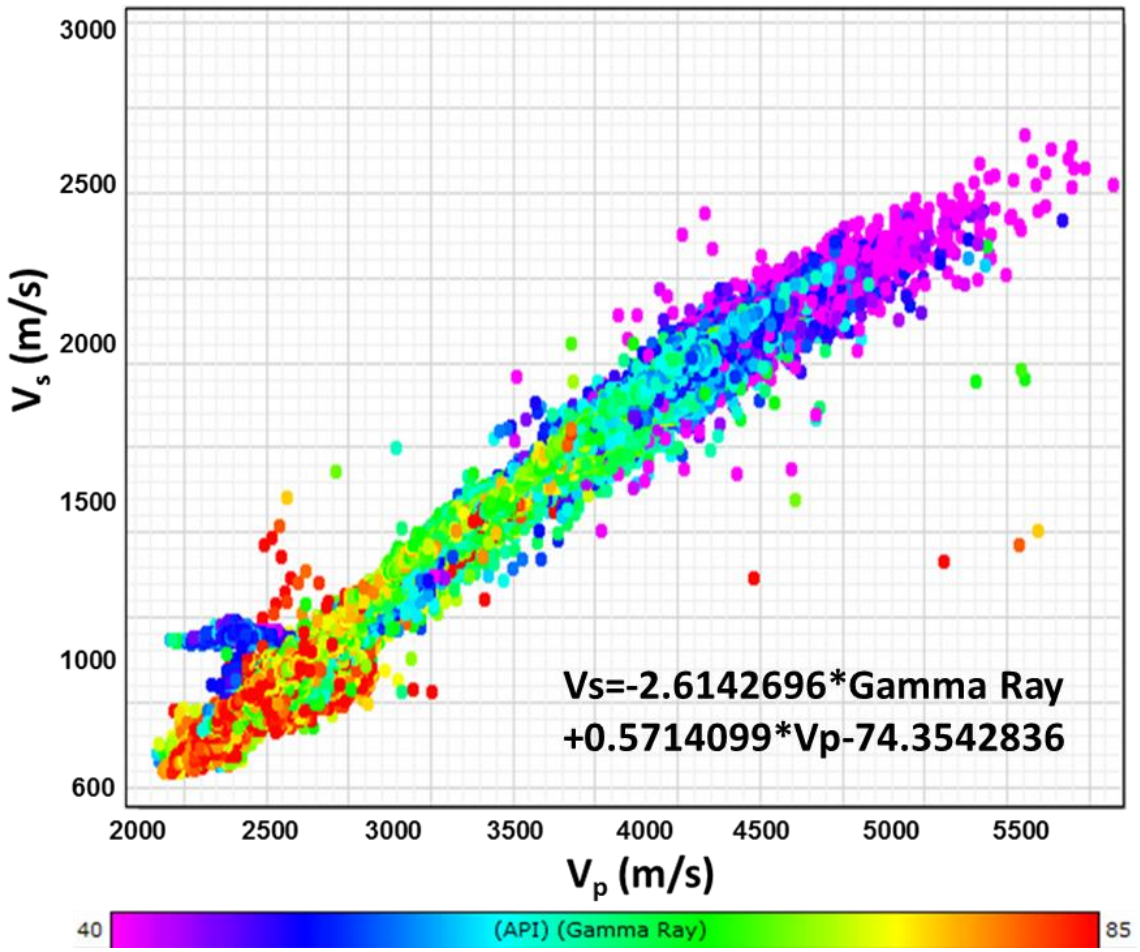

Figure 6.3. Relationship between gamma ray, V_p and V_s from well control in order to predict S-wave sonic logs where they do not exist. Five wells in the area having gamma ray and dipole sonic information are used for this plot.

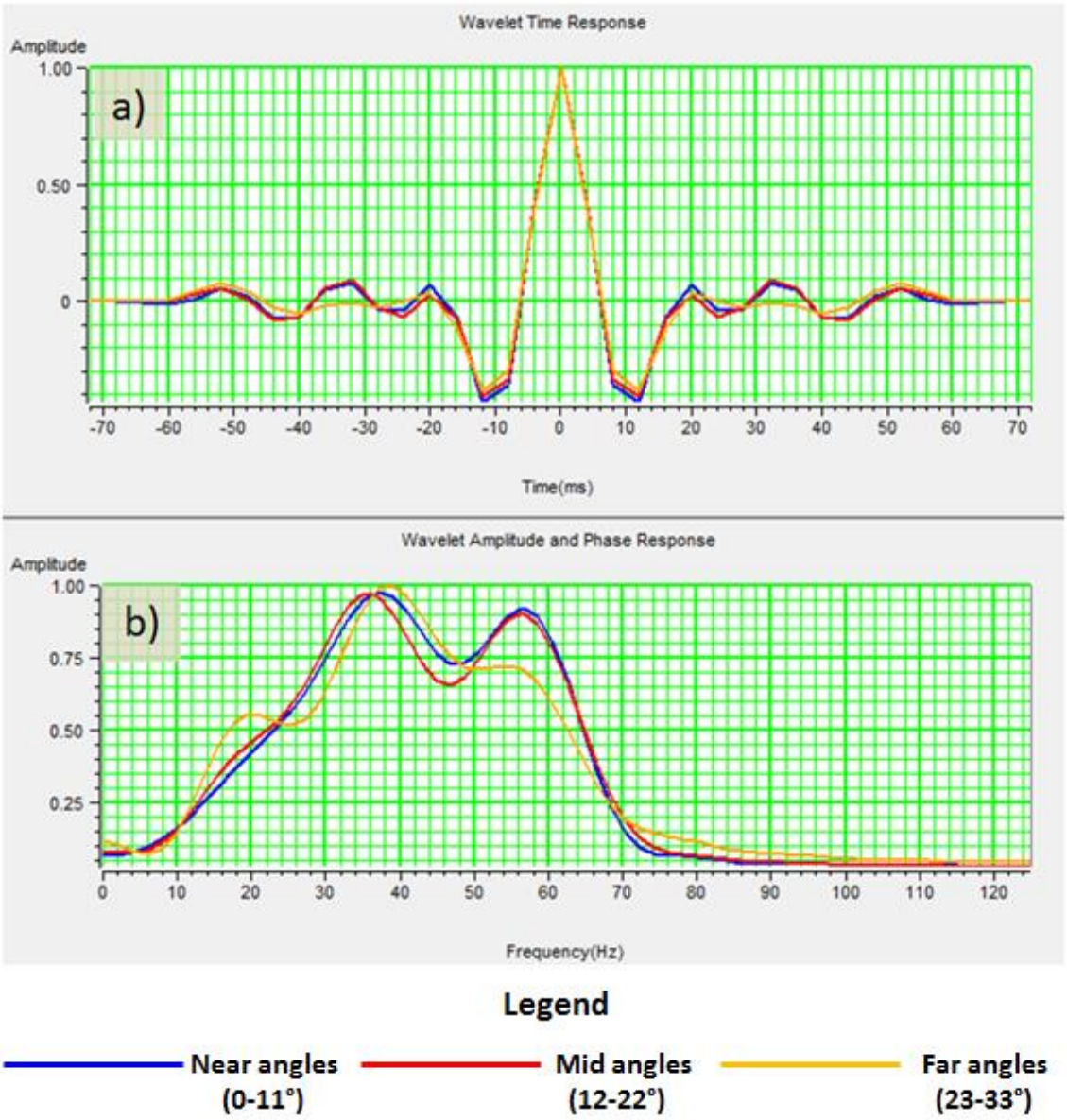

Figure 6.4. (a) Angle-dependent statistical wavelets extracted from the angle gathers and (b) their corresponding frequency spectra. Blue: near angles (0-11°); red: mid angles (12-22°); orange: far angles (23-33°).

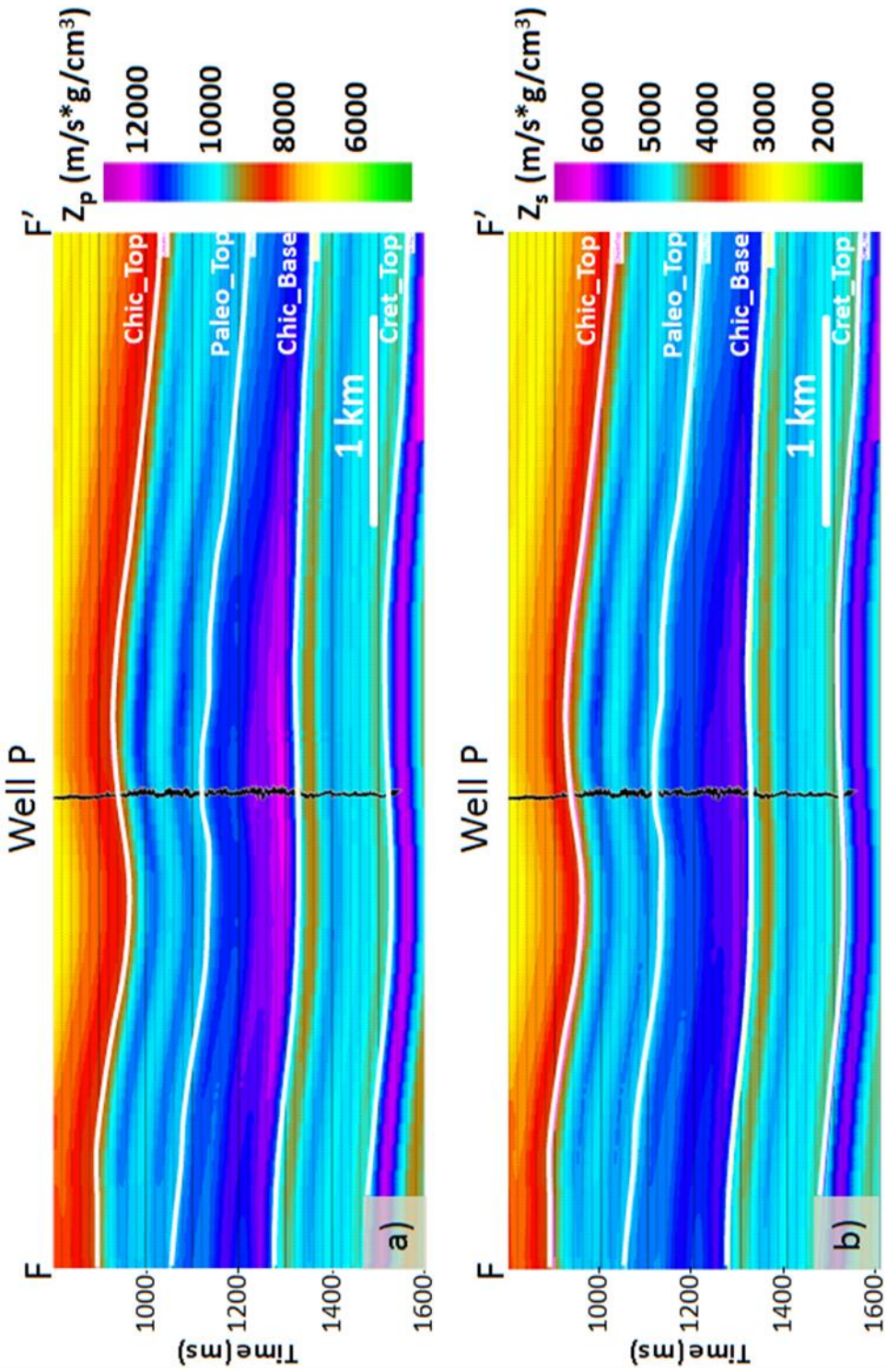

Figure 6.5. Low frequency models for (a) Z_p and (b) Z_s corresponding to line F-F'. Location shown in Figure 6.9.

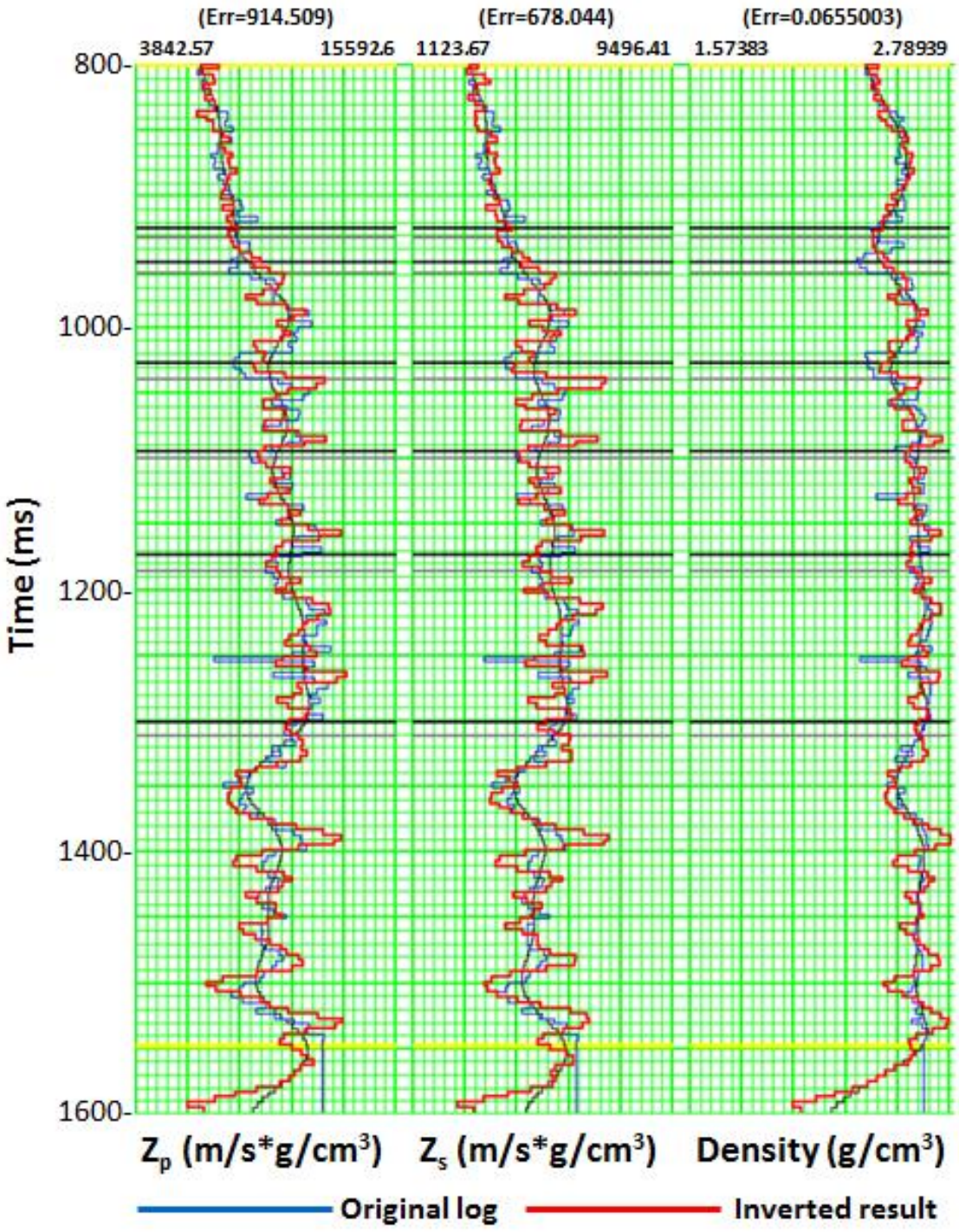

Figure 6.6. Comparison between the original well logs and inverted traces for Z_p, Z_s and density generated from simultaneous prestack inversion, at a well P. Location of the well is shown in Figure 6.9.

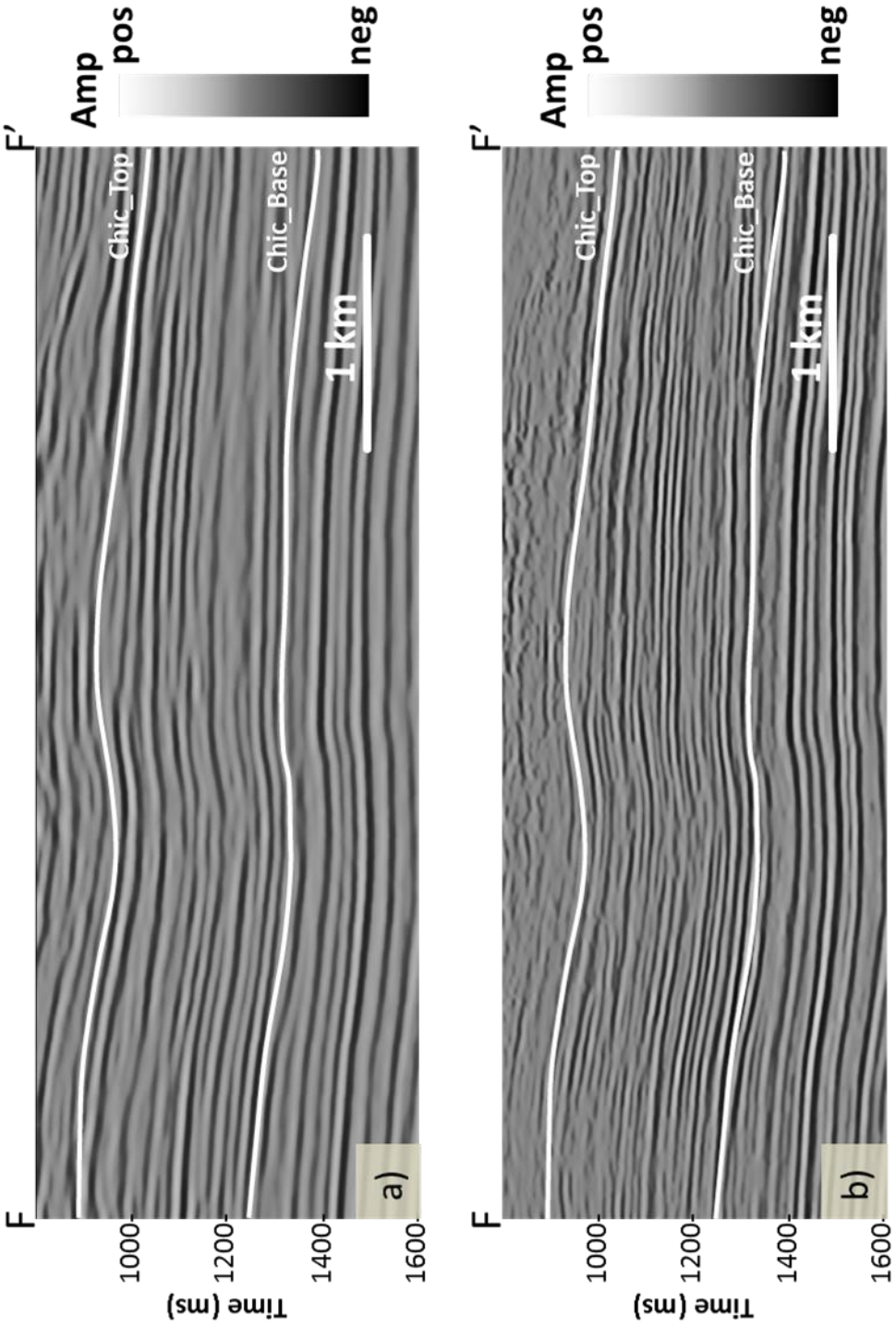

Figure 6.7. (a) Original prestack time migrated vertical seismic amplitude section and (b) the same section after prestack data conditioning. Note better definition of the units and improved resolution after data conditioning. Location shown in Figure 6.9.

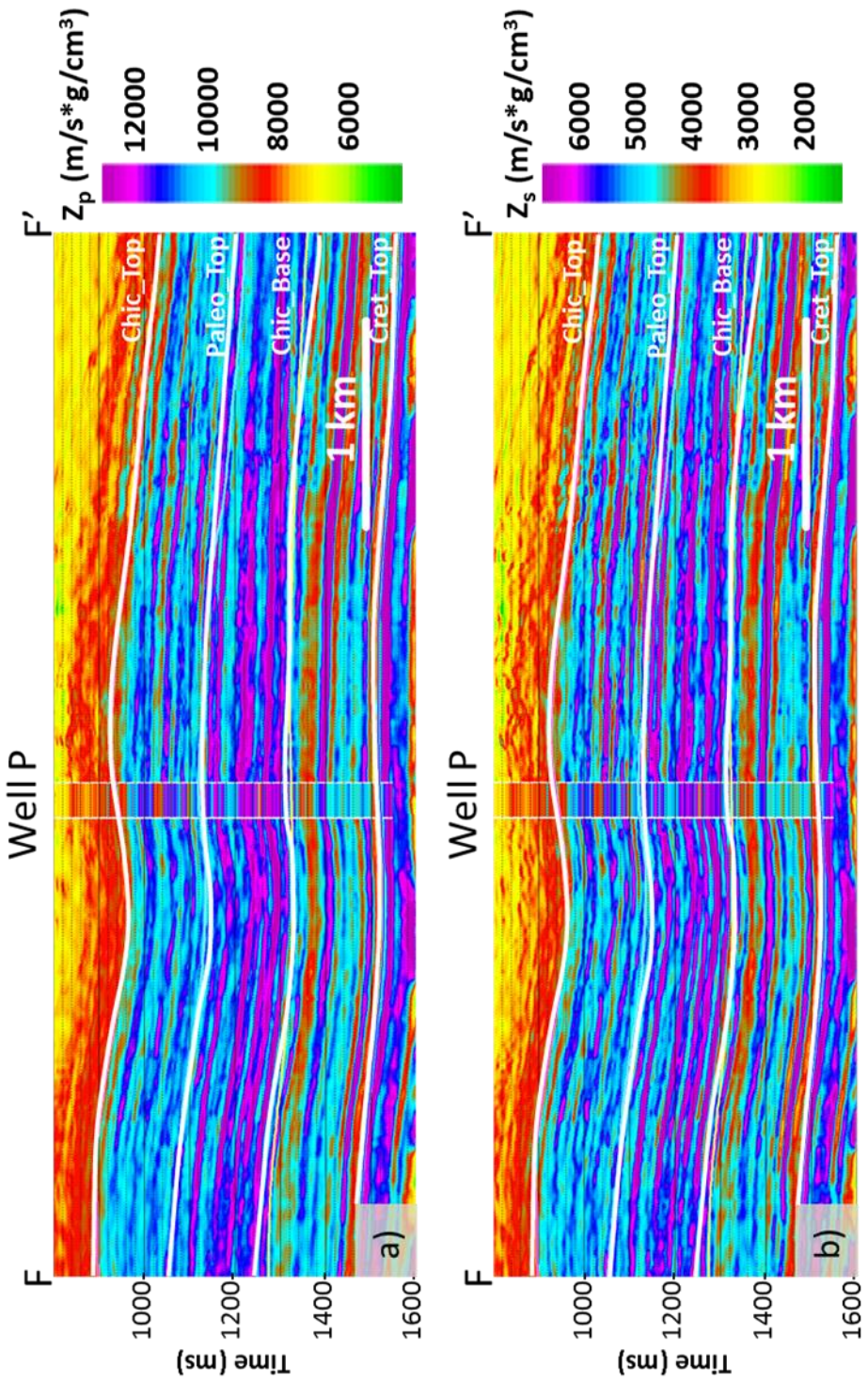

Figure 6.8. Vertical slices along line F-F' through the (a) Z_p and (b) Z_s volumes. Location shown in Figure 6.9. Note the good correlation between the Z_p and Z_s calculated from the well and the inverted result. Z_s provides higher resolution than Z_p.

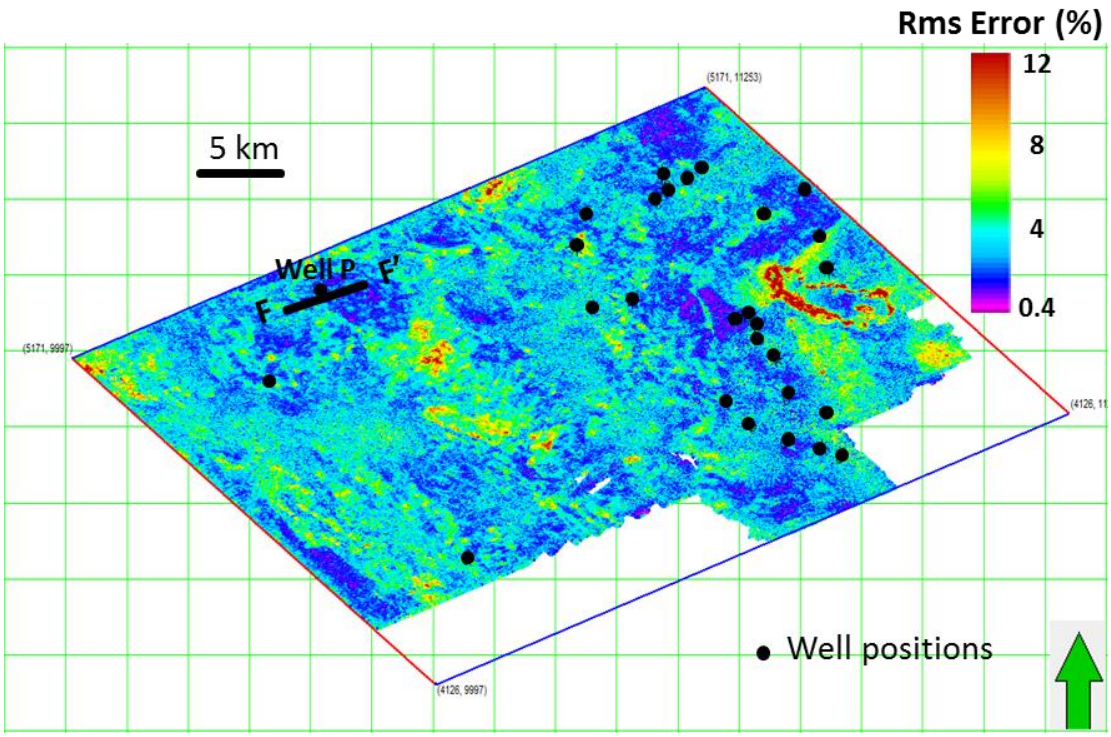

Figure 6.9. Normalized RMS error time slice at t= 1200 ms. Note relatively low error are observed near the wells.

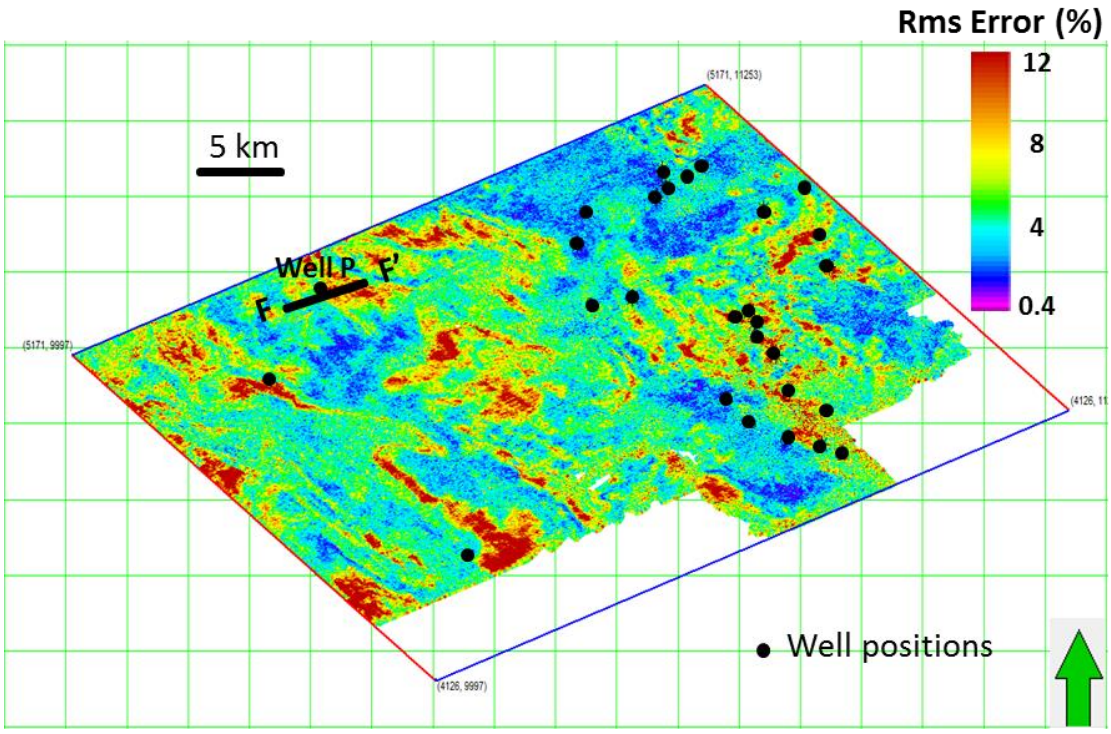

Figure 6.10. Normalized RMS error time slice at t= 1400 ms. Note relatively low error are observed near the wells. Lack of well control in the deeper section results in higher amount of error in the deeper time slice compared to the shallower time slice.

Conclusions

The integration of seismic attributes, seismic modeling, data reprocessing, and impedance inversion helps better image and understand the geological structure of the Chicontepec Basin. In the Amatitlán survey, similarity attributes are sensitive to faulting, but not sensitive to folding. On the other hand curvature attributes are sensitive to faulting as well as folding. Subtle faults with very small displacement may not be seen on coherence attribute volumes, whereas these features can be identified on curvature attribute volumes. A fault is commonly seen as a pattern on seismic attribute volumes. A low coherence anomaly appears on the fault plane, while curvature anomalies usually appear on either side of the fault. Multiattribute visualization works best when one attribute is plotted against gray scale and the other attribute is plotted against a polychromatic color bar. Co-rendering curvature with coherence provides a superior interpretation product, allowing us to visualize and quantify structural styles on seismic volumes. Folds and pop-up structures are better illuminated on horizon slices, while faults and chaotic zones are better illuminated on time slices. Disorder attribute delineates chaotic zones with poor data quality and provides a measure of horizon-picking confidence.

Synthetic seismic modeling confirms that pop-up and graben structures in the Chicontepec area give rise to coherence and curvature anomalies. Seismic modeling results are similar to those from the real data. Synthetic modeling gives us an idea of how the pop-up and graben structures in the area look like in reality. Specifically, it shows how continuous interbed multiples break up curvature and coherence anomalies that would otherwise be continuous.

Prestack data conditioning, which significantly improves data quality, is a crucial step for seismic inversion. Residual velocity analysis results in better vertical and lateral definition of units. Compared to the conventional NMO corrections, MPNMO corrections preserve more high frequency data and provide increased resolution by reducing the wavelet stretching effect at far offsets. Prestack structure oriented filtering refines the data by removing random noise and improving signal-to-noise ratio.

Prestack inversion provides a volumetric estimation of rock type, which allows the differentiation of shales and sandstone reservoirs in the area. For Amatitlán, the S-impedance (Z_s) volume provides higher resolution than the P-impedance (Z_p) volume. Well logs contain significant information for seismic inversion. After prestack inversion, relatively low error are observed near the wells compared to their surrounding environments.

References

Abbaszadeh, M., Ohno, K., Okano, H., 2008, Reservoir characterization and CO2-EOR injection studies in low permeability Chicontepec turbidite reservoirs, Mexico: Technical paper IPTC 12637 presented at International Petroleum Technology Conference, Kuala Lumpur, Malaysia.

Al-Dossary, S., and K. J. Marfurt, 2006, 3-D volumetric multispectral estimates of reflector curvature and rotation: Geophysics, **71**, P41–P51.

Al-Dossary, S. and Y. Wang, 2013, A new algorithm for the seismic disorder attribute: In Press.

Bermúdez, J., J. Araujo-Mendieta, M. Cruz-Hernández, H. Salazar-Soto, S. Brizuela-Mundo, S. Ferral-Ortega, and O. Salas-Ramírez, 2006, Diagenetic history of the turbiditic litharenites of Chicontepec Formation, northern Veracruz: Controls on the secondary porosity for hydrocarbon emplacement: Gulf Coast Association of Geological Societies Transactions, **56**, 65-72.

Bitter, M.R., 1993, The sedimentation and provenance of Chicontepec sandstones with implications for uplift of the Sierra Madre Oriental and Teziutlán Massif, East-Central Mexico: Proceedings 13th Annual SEPM Gulf Coast Section Reservoir Conference, Houston, 155-172.

Cantu Chapa, A., 2001, Mexico as the western margin of Pangea based on biostratigrapic evidence from the Permian to the Lower Jurassic, in Bartolini, C., Buffler, R. T., and Cantu-Chapa, A., eds., The Western Gulf of Mexico Basin-Tectonics, Sedimentary Basin, and Petroleum System: AAPG Memoir, no. 75, 1-28.

Chopra, S., and K. J. Marfurt, 2007, Seismic attributes for prospect identification and reservoir Characterization: Geophysical Developments, **11,** Society of Exploration Geophysicists.

Diaz, G., 2008, Sequence stratigraphy of Chicontepec Play, Tampico-Misantla Basin, Mexico: M.S. Thesis, The University of Oklahoma.

Goldhammer, R.K., and C. A. Johnson, 2001, Middle Jurassic-Upper Cretaceous paleogeographic evolution and sequence-stratigraphic framework of the northwest Gulf of Mexico rim, in Bartolini, C., Buffler, R. T., and Cantu-Chapa, A., eds., The Western Gulf of Mexico Basin-Tectonics, Sedimentary Basin, and Petroleum Systems: AAPG Memoir **75**, 45-81.

Ha, T., and K.J. Marfurt, 2013, Disorder attribute implementation on TX-LA dataset: Estimate horizon-picking confidence and map chaotic features, The University of Oklahoma, AASPI Annual Meeting.

Hampson, D. P., B. H. Russell, and B. Bankhead, 2005, Simultaneous inversion of pre-stack seismic data: Proceedings of the 75th Annual International Meeting of the SEG; Expanded Abstracts, 1,633-1,637.

Horbury, A. D., S. Hall, F. Gonzalez-P., D. Rodrıguez-F., A. Reyes-F., P. Ortiz-G., M. Martinez-M., and G. Quintanilla-R., 2003, Tectonic sequence stratigraphy of the western margin of the Gulf of Mexico in the late Mesozoic and Cenozoic: Less passive than previously imagined, in C. Bartolini, R. T. Buffler, and J. Blickwede, eds., The Circum-Gulf of Mexico and the Caribbean: Hydrocarbon habitats, basin formation, and plate tectonics: AAPG Memoir **79**, 184–245.

Kwiatkowski, J. T., and K.J. Marfurt, 2011, Data conditioning of legacy pre-stack time migrated gathers from the Mid-Continent: Abstract volume of the AAPG Mid Continent Section Meeting.

Luo, Y., W. G. Higgs, and W. S. Kowalik, 1996, Edge detection and stratigraphic analysis using 3D seismic data: 66th Annual International Meeting, SEG, Expanded Abstracts, 324-327.

Mai, H. T., 2010, Seismic attribute analysis and its application to mapping folds and fractures: PhD Dissertation, The University of Oklahoma.

McQuillan, H., 1974, Fracture patterns on Kuh-e Asmari anticline, southwest Iran: AAPG Bulletin, **58**, 236–246.

Morán-Zenteno, D., 1994, Geology of the Mexican Republic: AAPG Studies in Geology, no. 39, 160 p.

Murray, Jr., G. H., 1968, Quantitative fracture study-Spanish Pool, McKenzie County, North Dakota: AAPG Bulletin, **52**, 57–65.

Lisle, R. J., 1994, Detection of zones of abnormal strains in structures using Gaussian curvature analysis: AAPG Bulletin, **78**, 1811-1819.

Pena-Marino, V., 2010, Integrated geophysical investigation of shallow igneous bodies and the impact on seismic data quality, Chicontepec Basin, Mexico: M.S. Thesis, The University of Oklahoma.

Roberts, A., 2001, Curvature attributes and their application to 3D interpreted horizons: First Break, **19**, 85-99.

Salvador, A., 1991, Origin and development of the Gulf of Mexico Basin, in Salvador, A. ed., The Gulf of Mexico Basin, The Geology of North America, v. J: DNAG (Decade of North American Geology), Geological Society of America, 389-444.

Sarkar, S., 2011, Depositional history and reservoir characteristics of structurally confined foredeep turbidites, northern Chicontepec Basin, Mexico: PhD Dissertation, The University of Oklahoma.

Stewart, S. A., and T. J. Wynn, 2000, Mapping spatial variation in rock properties in relationship to scale-dependent structure using spectral curvature: Geology; **28**, 691–694.

Swisi, A., 2009, Post- and Pre-stack attribute analysis and inversion of Blackfoot 3D seismic dataset: M.S. Thesis, The University of Saskatchewan.

Zhang, B., K. Zhang, S. Guo, and K. J. Marfurt, 2013, Nonstretching NMO correction of prestack time-migrated gathers using a matching-pursuit algorithm: Geophysics, **78**, U9-U18.